

# Emergent Outlier View Rejection in Visual Geometry Grounded Transformers

Jisang Han<sup>1,2†\*</sup> Sunghwan Hong<sup>3\*</sup> Jaewoo Jung<sup>1</sup> Wooseok Jang<sup>1</sup> Honggyu An<sup>1</sup>  
 Qianqian Wang<sup>4</sup> Seungryong Kim<sup>1†</sup> Chen Feng<sup>2†</sup>

<sup>1</sup>KAIST AI <sup>2</sup>New York University <sup>3</sup>ETH AI Center, ETH Zurich <sup>4</sup>UC Berkeley  
<https://cvlab-kaist.github.io/RobustVGGT>

## Abstract

*Reliable 3D reconstruction from in-the-wild image collections is often hindered by “noisy” images—irrelevant inputs with little or no view overlap with others. While traditional Structure-from-Motion pipelines handle such cases through geometric verification and outlier rejection, feed-forward 3D reconstruction models lack these explicit mechanisms, leading to degraded performance under in-the-wild conditions. In this paper, we discover that the existing feed-forward reconstruction model, e.g., VGGT, despite lacking explicit outlier-rejection mechanisms or noise-aware training, can inherently distinguish distractor images. Through an in-depth analysis under varying proportions of synthetic distractors, we identify a specific layer that naturally exhibits outlier-suppressing behavior. Further probing reveals that this layer encodes discriminative internal representations that enable an effective noise-filtering capability, which we simply leverage to perform outlier-view rejection in feed-forward 3D reconstruction without any additional fine-tuning or supervision. Extensive experiments on both controlled and in-the-wild datasets demonstrate that this implicit filtering mechanism is consistent and generalizes well across diverse scenarios.*

## 1. Introduction

Multi-view 3D reconstruction [18, 41], the task of recovering scene geometry and camera poses from images with overlapping views, has been a central problem in computer vision, enabling applications across autonomous systems [64], scene understanding [10, 28, 44, 63] and AR/VR [29]. As these applications scale, they demand reconstructions that are accurate, efficient, and robust across diverse capture conditions.

<sup>‡</sup>Work done during a visiting research stay at New York University.

<sup>\*</sup>Equal contributions.

<sup>†</sup>Co-corresponding and equal advising.

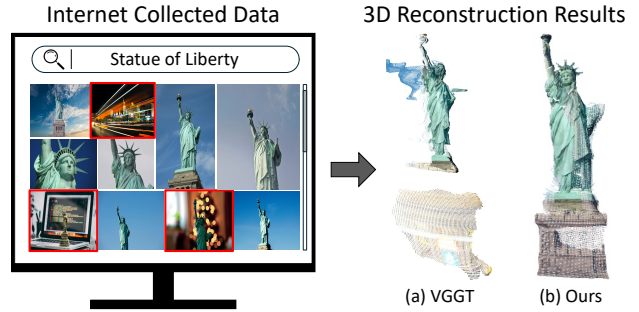


Figure 1. **Motivation.** In practice, image sets gathered for 3D reconstruction, e.g., via keyword search, often contain distractors or entirely irrelevant photos. As illustrated in (a), leaving these images unfiltered contaminates the VGGT [56] pipeline, producing noisy geometry and visible artifacts in the final reconstruction. In contrast, our **training-free** approach, dubbed RobustVGGT, filters views using internal representations within VGGT [56], yielding cleaner, more stable reconstructions, as shown in (b).

Recent feed-forward reconstruction models [30, 55, 57] have made significant progress in this task by predicting geometry directly from image sets using learned representations and attention mechanisms. In particular, models such as VGGT [56] and Pi3 [58] bypass many iterative components of classical pipelines [15, 38, 53], achieving impressive speed and strong performance on curated benchmarks.

A missing piece, however, is robustness to image collections with *noisy or irrelevant views*. In practical settings, image collections often contain distractors, off-topic frames, occlusions, or transient objects. This arises in a variety of scenarios, from casual captures and community photo collections to keyword-based queries e.g., “Statue of Liberty”, as exemplified in Fig. 1. These models [56, 57] lack an explicit mechanism to identify and remove inconsistent views; consequently, distractors can pass through the feed-forward pipeline, biasing pose estimation and degrading the recovered 3D structure (see Fig. 1(a)).

Classical Structure-from-Motion (SfM) pipelines address this challenge through stage-wise filtering and verifi-

cation. After image retrieval [3], local features are detected and matched [11, 13, 31], and mismatches are pruned via robust estimation and geometric checks [15, 18], followed by bundle adjustment [53]. Systems like COLMAP [41] include these multi-stage procedures and are resilient to outlier views. However, they rely on iterative optimization and modular stages, which can limit scalability and tight integration with learning-based pipelines.

Our key insight is that VGGT [56], despite lacking explicit outlier rejection mechanism or noise-aware training, can be *repurposed for robust view selection* by leveraging an emergent properties of their internal representations: attention maps and intermediate features naturally emphasize spatially relevant, 3D-consistent views while downweighting distractors, *without* fine-tuning, retraining or modifying the model. Through controlled analysis, we observe that certain layer in VGGT consistently suppress views that are inconsistent with the scene geometry.

Building on this observation, we introduce a simple scoring scheme, called **RobustVGGT**, that quantifies per-view relevance using these internal signals and filters distractors with a single fixed threshold that generalizes across diverse datasets. This procedure introduces *no additional parameters or supervision* and improves robustness while *preserving* the efficiency of feed-forward reconstruction. We evaluate our framework on real-world datasets [36, 39, 42, 47]. Despite its simplicity, our method consistently outperforms all compared baselines across datasets and different noise levels. We also provide ablations and analyses to validate our design choices.

Our contributions include:

- For the first time, we reveal an emergent noise-suppressing behavior in VGGT’s internal attention and feature representations through layer-wise quantitative and qualitative analyses.
- We propose a simple, training-free filtering mechanism that requires no architectural changes and selects geometrically consistent views by thresholding internal attention/feature signals with a single global parameter shared across datasets.
- We demonstrate consistent gains over strong baselines across diverse benchmarks and noise settings.

## 2. Related work

**Tabula rasa 3D reconstruction.** Structure from Motion (SfM) is a long-standing problem in computer vision that aims to estimate camera parameters and reconstruct 3D structure from multiple images of a static scene captured from different viewpoints. Traditional SfM pipelines [1, 18, 41, 48] comprise multiple stages—keypoint detection and description [11, 13, 31, 38, 52], matching [8, 9, 14, 20–22, 40, 49], triangulation [19], outlier filtering [4, 5, 7, 59] and bundle adjustment [53]—that jointly refine both struc-

ture and camera poses through iterative optimization. A key advantage of these pipelines is their robustness to noisy or irrelevant images or points: stages such as geometric verification, epipolar consistency checks, and RANSAC-based outlier rejection [4, 15] effectively filter mismatched features and erroneous correspondences before final reconstruction. Frameworks like COLMAP have become standard for reliable large-scale 3D reconstruction under such mechanisms. In contrast, recent feed-forward 3D reconstruction models (e.g., VGGT [56]) omit explicit filtering and can degrade on web-sourced, in-the-wild image sets with distractors. However, we show these models still exhibit *implicit* outlier-suppression signals; by probing such layers and leveraging them at inference to select/reject views, we improve robustness without reinstating a full SfM pipeline.

**Learning-based 3D reconstruction.** Learning-based multi-view 3D reconstruction has largely advanced through cost volumes that infer per-view depth followed by fusion. Supervised methods [16, 54, 61, 62] achieve strong accuracy on curated benchmarks but typically assume clean inputs and rely on view selection heuristics rather than explicit outlier rejection. To reduce annotation needs, weak/self-supervised approaches embed geometric consistency into the training or inference loop, e.g., differentiable BA or video-to-depth formulations [50, 51], yet these still tend to degrade with distractor views common in web-sourced collections. Many pipelines [17, 23, 24, 57] also rely on COLMAP [41] for camera poses, supervision, or geometric verification during training/evaluation. More recent feed-forward correspondence/pointmap models [2, 30, 56, 57] bypass iterative SfM modules and produce geometry directly, but they do not include explicit geometric verification. Our work complements this line by probing a feed-forward architecture, showing that internal layers encode signals correlated with outlier suppression, and leveraging them to select/reject views for more robust reconstruction under in-the-wild noise.

**Image retrieval and visual place recognition.** Multi-view 3D reconstruction from web-sourced photo collections typically begins with keyword queries (e.g., “Rome”), followed by image retrieval or VPR to identify candidate views. Early approaches use bag-of-words [32, 46] or VLAD-based encoding [25], while more recent systems adopt learned descriptors such as NetVLAD [3], GeM [35], MegaLoc [6] and DELF [33]. These methods are widely used in retrieval-based SfM pipelines and are integrated into systems like COLMAP [41] to initialize the view graph. However, retrieval similarity may not always reflect geometric suitability, and distractor images can persist. Our method provides a complementary mechanism by probing the internal layers of feed-forward 3D reconstruction models to identify and downweight distractors, improving ro-



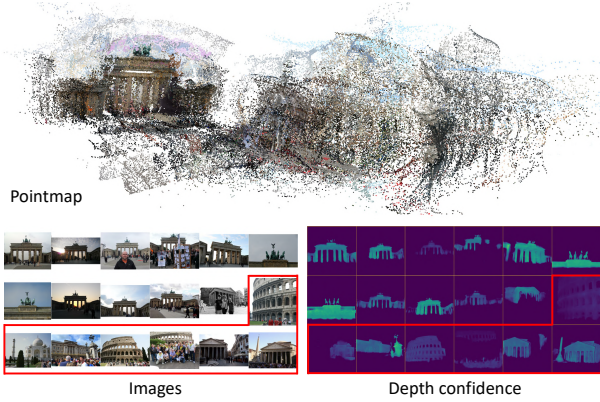


Figure 2. **Reconstruction by VGGT [56].** Although VGGT predicts per-pixel confidence maps to down-weight unreliable depths, this post-hoc signal operates only at the point level and does not filter views. Consequently, distractor images are still reconstructed, allowing spurious content to corrupt the recovered geometry.

bustness in uncured image sets.

### 3. Method

#### 3.1. Preliminaries

Feed-forward 3D reconstruction models [30, 56, 57] aim to recover scene geometry and camera poses directly from a set of  $N$  images  $\{I_1, \dots, I_N\}$  without relying on explicit feature matching or optimization. These models learn to predict either per-view depth and pose  $(D_i, \mathcal{P}_i)$  or pointmaps  $X_i$  by first extracting image features and then modeling cross-view relationships using attention-based modules. Geometry is recovered by either regressing  $X_i$  directly or unprojecting  $D_i$  using estimated poses  $\mathcal{P}_i$ , with per-point confidence  $C_i$  optionally predicted. A representative model is the VGGT [56], which uses a transformer-based encoder and alternating attention layers that consist of frame-wise and global attention to feed to dedicated decoder heads to estimate  $\mathcal{P}_i$  and  $D_i$ , along with a dedicated head for direct  $X_i$  regression. VGGT is trained end-to-end using supervision signals including camera pose loss, depth regression, and pointmap confidence, and outputs  $\mathcal{P}_i, X_i, C_i$  in a single pass of inference.

#### 3.2. Motivation and overview

Feed-forward 3D reconstruction models, such as DUST3R [57], VGGT [56], and Pi3 [58], directly estimate scene geometry and camera poses from unstructured image collections, offering an efficient alternative to traditional SfM pipelines [41]. However, a critical limitation—often overlooked in practice and unexplored—is the absence of explicit mechanisms for filtering noisy or irrelevant input views. This becomes especially pronounced in practical settings, where image collections frequently

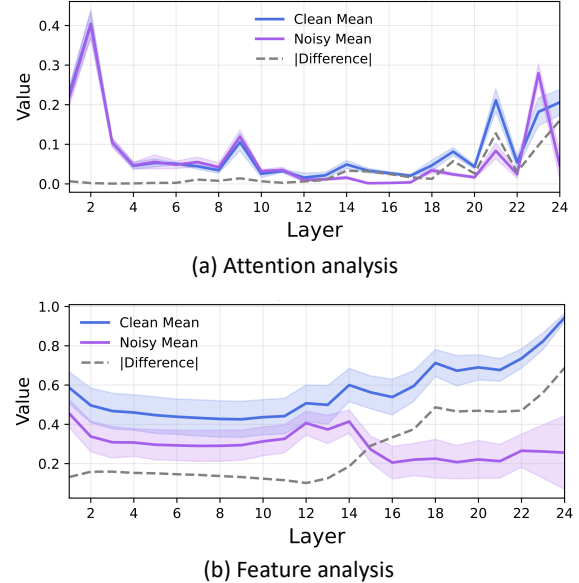


Figure 3. **Layer-wise analysis.** We measure the gap between clean and distractor views for attention and feature similarity across VGGT’s all layers. The separation grows with depth and peaks at the final layer, indicating emergent noise suppression.

include off-topic scenes, or occlusions. Without built-in outlier rejection stages, such as view-graph construction or geometric verification [3, 41], these models remain vulnerable to distractor views, leading to degraded pose and geometry (see Fig. 10).

A common mitigation is to pre-filter with visual place recognition (VPR) or retrieval-based methods to prune distractors before reconstruction, following conventional SfM practice [41]. While common, such approaches typically require per-scene hyperparameter tuning, and may not directly generalize across datasets or domains. Another seemingly reasonable option is to leverage the per-point confidence scores predicted with each pointmap to discard unreliable 3D points. Unfortunately, these confidences act *post hoc* at the point level; without an explicit view-filtering mechanism, the system still reconstructs *all* images, allowing distractor views to degrade poses and geometry, as shown in Fig. 2.

In contrast, we observe *an important emergent property*: VGGT [56], despite being trained without any explicit outlier labels or filtering objectives, exhibits an emergent form of view selectivity in its internal representations. In particular, later-stage representations consistently downweight distractor views while emphasizing geometrically consistent ones. This insight enables a simple, training-free filtering strategy that leverages VGGT’s own attention/feature scores to rank and select views—eliminating additional modules, retraining, or hand-tuned retrieval pipelines—and yields robust scene geometry recovery from image collections con-

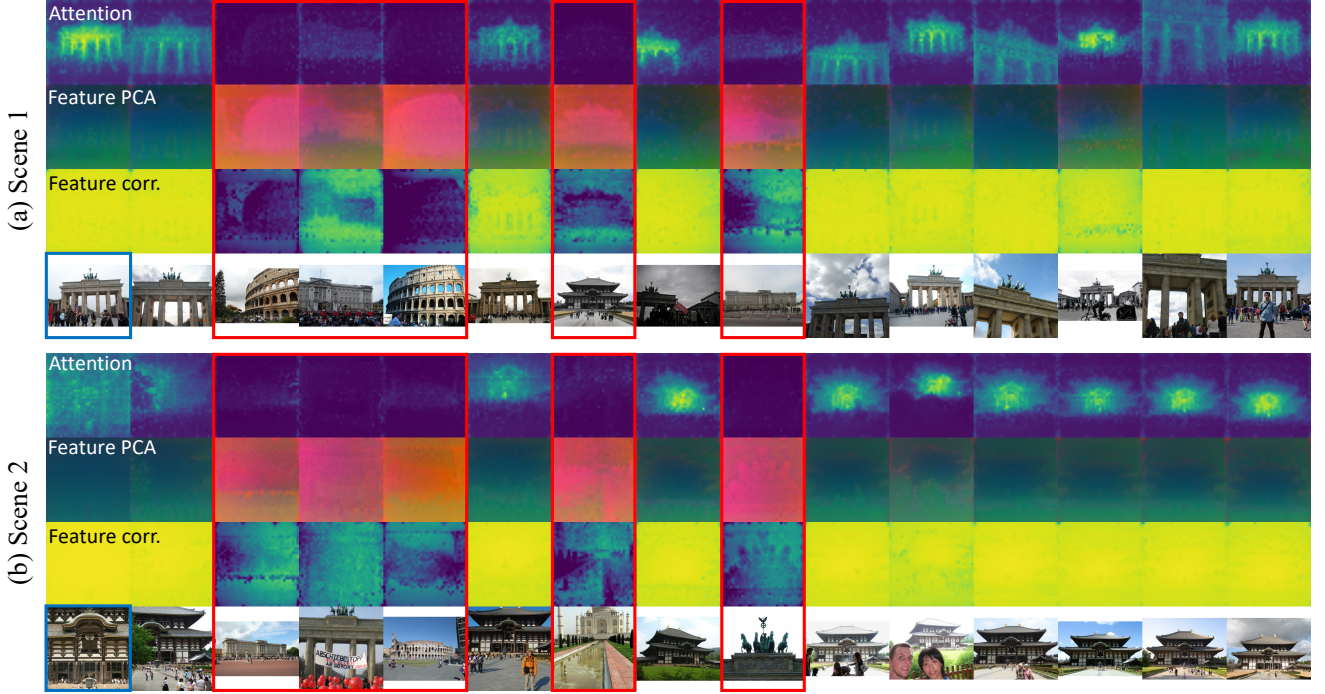


Figure 4. **Feature/attention visualization.** We show cross-view attention maps and intermediate feature–similarity maps from the final layer of VGGT on mixed sets containing clean and distractor images. Distractors are marked with red boxes; the query image is marked with a blue box. For each context image, scores are computed with respect to the query, averaged over all query tokens, and normalized for display. Both probes clearly downweight distractor views, revealing the model’s emergent view selectivity.

sisting of noisy images.

The remainder of this section is structured as follows. In § 3.3, we formulate the view selection problem in the context of multi-view feed-forward reconstruction. In § 3.4, we begin with a pilot study to investigate the respective roles of feature and attention maps and identify the key layer critical for view selection. Building on this, in § 3.5 we introduce internal representation-based view filtering approach.

### 3.3. Problem formulation

Given a set of  $N$  uncalibrated images  $\{I_1, I_2, \dots, I_N\}$  capturing a static scene, the objective is twofold: (1) to estimate the 3D scene structure and camera parameters, and (2) to identify and discard noisy or irrelevant views that could degrade the reconstruction quality. Following the formulation of VGGT [56], our model still predicts, for each image  $I_i$ , a camera pose  $\mathcal{P}_i$ , a per-pixel depth map  $D_i$ , and a 3D pointmap  $X_i$ , computed by lifting  $D_i$  into 3D space using  $\mathcal{P}_i$ . Additionally, the model outputs a confidence map  $C_i$  associated with each pointmap.

To enhance robustness to distractors, we aim to extract a clean subset of context images  $\{I_j\}_{j \in \phi(i)} \subset \{I_1, \dots, I_N\}$  for an arbitrary query image  $I_i$ . This is achieved by leveraging VGGT’s internal representations—intermediate feature maps  $F_i$  and cross-view attention weights  $A_{i \rightarrow j}$ —where  $A_{i \rightarrow j}$  is obtained from dot-product attention between query

and key projections. We define a selection function  $\phi(i)$  that retains only the clean views  $I_j$ . The filtered context set  $\{I_j\}_{j \in \phi(i)}$  is then *re-fed* into the model to produce the final predictions  $(\mathcal{P}_i, D_i, X_i)$  using only the most geometrically consistent views.

### 3.4. Emergent noise suppression abilities

We probe the internal representations of VGGT [56] to understand how it handles distractor views. To this end, we isolate the alternating attention stack and analyze, layer by layer, both the intermediate feature maps and the corresponding attention maps produced for a given image set.

**Deconstructing VGGT: Internal representations.** Although feed-forward 3D reconstruction models like VGGT do not explicitly implement outlier rejection, we find that they exhibit *emergent* filtering behavior in their internal representations, such as features and attention. Concretely, given a query image and a set of context images containing both clean and distracting views, we compute for each alternating-attention layer: (i) an attention score obtained by aggregating the weight that the query image that a user sets assigns to each context image, and (ii) the cosine similarity between the query feature map and each context feature map, which is computed pixel-wise on  $\ell_2$ -normalized features and then averaged over pixels to yield a single scalar per pair. We repeat this across layers and report, for

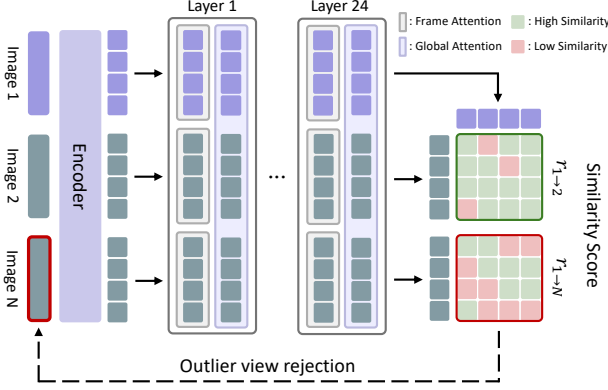


Figure 5. **Framework overview.** We compute per-view relevance from VGGT’s internal representations using two probes: (i) cross-view attention from query–key projections and (ii) cosine similarity of intermediate dense features. The resulting score  $r_{i \rightarrow j}$  is thresholded with a single global  $\tau$  to filter distractors, and the filtered set is re-fed to VGGT for reconstruction—without retraining or architectural changes.

each layer, the average scores for clean pairs and for distractor pairs, along with their gap (clean minus distractor), as shown in Fig. 3.

From Fig. 3(a), early layers show little separation between clean and distractor views; the gap grows steadily and peaks in the final layer, indicating that the model increasingly differentiates useful from irrelevant views as reasoning deepens. A parallel analysis on the feature maps reveals a similar trend with an even larger separation, as shown in Fig. 3(b), suggesting that late-layer features act as a stronger discriminator of geometric relevance. Together, these findings support that the last layer serves as a critical gate that distinguishes views inconsistent with the query’s geometry. Notably, this behavior emerges without any supervision for outlier filtering, plausibly as a byproduct of optimizing for multi-view geometric consistency.

**Qualitative evidence.** Fig. 4 visualizes attention and feature responses, as well as the cosine similarity between feature responses, from the final layer. Irrelevant frames (e.g., images from non-dominant scenes or with severe occlusions) receive low attention weight and weak feature similarity, whereas geometrically consistent views remain highly activated. These qualitative results align with the quantitative layer-wise trends and indicate that VGGT’s internal representations inherently distinguish distracting tokens and views. Motivated by this observation, our method leverages these late-layer similarity signals as a natural cue for identifying uninformative views.

### 3.5. Outlier view rejection

We realize the selection function  $\phi(i)$  using *only* internal representations in VGGT [56], acquired from a single feed-

forward. As seen in the Fig. 5, for a query (anchor) image  $I_i$ , we score each context image  $I_j$  by aggregating cross-view attention or intermediate feature similarity on the final layer  $\mathcal{L}$ .

**Attention score.** Let  $\ell^*$  be the final attention layer and  $A^{(\ell^*)}$  the multi-head averaged attention. For a query (anchor) image  $I_i$ , the per-image attention score is the simple mean over tokens of  $I_j$ :

$$r_{i \rightarrow j}^{\text{att}} = \frac{1}{HW} \sum_{u,v} A_{i \rightarrow j}^{(\ell^*)}(u, v), \quad (1)$$

where  $u, v$  indicate 2D spatial positions.

**Feature similarity score.** Let  $F_i^{(\ell^*)}, F_j^{(\ell^*)} \in \mathbb{R}^{H \times W \times d}$  be intermediate feature maps for images  $I_i$  and  $I_j$  from the same final layer. To measure feature-level similarity between two images, we first compute a pixel-wise correlation map [37] across all spatial positions of  $l-2$  normalized feature maps  $\tilde{F}_i^{(\ell^*)}(u), \tilde{F}_j^{(\ell^*)}(v)$ :

$$C_{i \rightarrow j}(u, v) = \tilde{F}_i^{(\ell^*)}(u) \cdot \tilde{F}_j^{(\ell^*)}(v), \quad (2)$$

where  $u$  and  $v$  index the  $\tilde{F}_i$  and  $\tilde{F}_j$ . The overall feature similarity score is obtained by spatially averaging all correlations:

$$r_{i \rightarrow j}^{\text{feat}} = \frac{1}{HW} \sum_{u,v} C_{i \rightarrow j}(u, v). \quad (3)$$

This corresponds to computing the mean cosine similarity over the entire  $HW \times HW$  correlation map.

**View rejection.** Based on these, we introduce two strategies for view rejection: **RobustVGGT-A**, which integrates attention-based scores, and **RobustVGGT-F**, which utilizes feature similarity scores. The context set for  $I_i$  is then

$$\phi(i) = \{j \mid j = i \text{ or } r_{i \rightarrow j}^O \geq \tau^O\}, \quad (4)$$

with  $O \in \{\text{att}, \text{feat}\}$  and a single fixed  $\tau^O$  shared across all benchmarks. We finally re-run the backbone on  $\{I_j\}_{j \in \phi(i)}$  to obtain  $(\mathcal{P}_i, D_i, X_i, C_i)$  using only spatially and geometrically consistent views.

## 4. Experiments

### 4.1. Experimental settings

**Datasets.** We evaluate across four benchmarks to cover web-sourced noise, casual captures and explicit distractors. Phototourism [26] comprises Internet-sourced image collections with large appearance changes (lighting, weather) and transient objects; we use six landmark scenes: Brandenburg Gate, Buckingham Palace, Colosseum, Pantheon, Taj Mahal, and Temple Naraa to assess robustness under real-world variability. On-the-go [36] contains casually captured



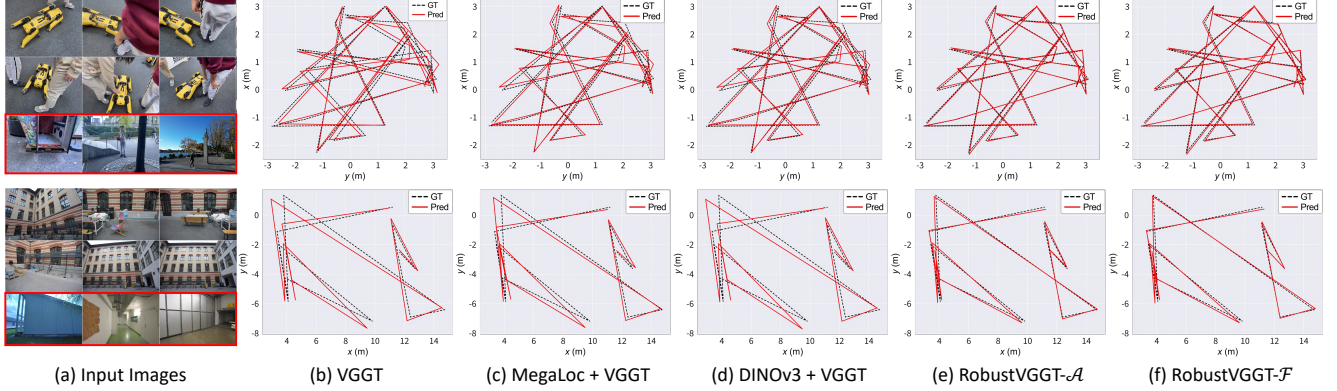


Figure 6. **Qualitative results of camera trajectory prediction.** Best viewed when zoomed in.

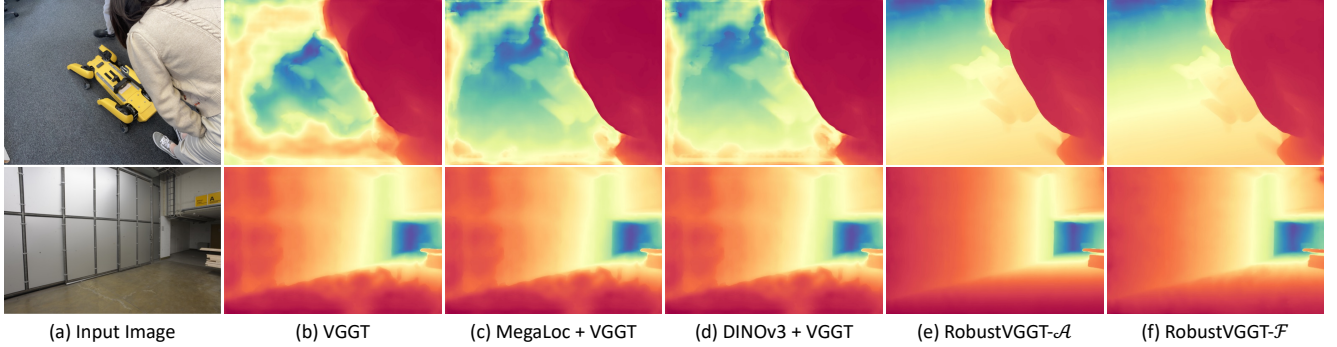


Figure 7. **Qualitative results of multi-view depth estimation.**

indoor/outdoor sequences with motion blur, occlusions, and uneven viewpoint coverage; we evaluate nine sequences: corner, drone, fountain, mountain, patio, patio\_high, spot, statue, and train. RobustNeRF [39] augments scenes with distractor images, providing a controlled testbed for outlier rejection. Following prior work [56], we also report results on ETH3D [43], a high-quality multi-view benchmark with accurate ground-truth poses and depth for assessing geometric precision.

**Task and baselines.** We assess our method on two downstream tasks—multi-view pose estimation and multi-view depth estimation—which jointly gauge the fidelity of the recovered 3D scene. We compare against VGGT [56] and against MAST3R-SfM [12], which reconstructs by building a view/scene graph from MAST3R encoder features and optimizing over it. In addition, we instantiate three VGGT-based pre-filtering baselines that apply view selection *before* running VGGT: (i) MegaLoc+VGGT uses an off-the-shelf visual place recognition model [6] to filter distracting images and passes the resulting context set  $\phi(i)$  to VGGT; (ii) DINOv3+VGGT replaces VPR with DINOv3 [45] global descriptors to select views; (iii) DINOv2<sup>†</sup>+VGGT leverages the VGGT encoder’s DINO-v2 [34] features for view selection.

**Evaluation protocol.** To our knowledge, this is the first work to evaluate feed-forward reconstruction under controlled *view-noise* levels, so we introduce a simple, reproducible protocol with three settings, *Small*, *Medium*, and *Large*, that differ only in the number of distractor images. For each trial, we sample  $N_c = 30$  **clean** images from the same scene and  $N_n \in \{10, 30, 50\}$  **distracting** images uniformly from *other* scenes, yielding sets of size  $N_c + N_n \in \{40, 60, 80\}$ . The sampling is repeated 10 times with different seeds, and we report mean over trials. All methods are evaluated on the *identical* sampled sets for fairness. For ETH3D [43], some scenes contain fewer images; we therefore set  $N_c=14$  and use  $N_n \in \{5, 14, 30\}$  for the Small/Medium/Large settings, respectively. In all datasets, clean and distracting pools are disjoint, and selection is scene-agnostic, which means no metadata or geometry is used. The same protocol is used for both evaluation tasks, multi-view pose and depth, and the noise level is the only factor varied across settings.

## 4.2. Experimental results

**Camera pose estimation.** We evaluate trajectories using three standard metrics: ATE, a Sim(3)-aligned RMSE of camera centers,  $RPE_{trans}$  and  $RPE_{rot}$ , translational/rotational errors between consecutive frames. We report mean metrics



Table 1. **Camera pose estimation across noise levels.** \* denotes per-dataset hyperparameter tuning with *oracle knowledge* of the number of clean images in the test set; these entries are shaded as they are not directly comparable. † uses DINOv2 features extracted from VGGT.

Methods	Small			Medium			Large			Avg		
	ATE ↓	RPE <sub>trans</sub> ↓	RPE <sub>rot</sub> ↓	ATE ↓	RPE <sub>trans</sub> ↓	RPE <sub>rot</sub> ↓	ATE ↓	RPE <sub>trans</sub> ↓	RPE <sub>rot</sub> ↓	ATE ↓	RPE <sub>trans</sub> ↓	RPE <sub>rot</sub> ↓
<b>Phototourism</b>												
MASt3R-SfM [12]	1.3556	2.4084	12.2887	1.2683	2.4735	11.9315	1.2329	2.3143	11.2861	1.2856	2.3987	11.8354
VGGT [56]	0.3068	0.4553	0.9906	0.3612	0.5314	1.1987	0.3833	0.5649	1.3304	0.3504	0.5172	1.1732
MegaLoc [6]+VGGT [56]	0.2735	0.4076	0.8841	0.2999	0.4460	0.9872	0.3161	0.4700	1.0714	0.2965	0.4412	0.9809
MegaLoc* [6]+VGGT [56]	0.2689	0.4013	0.8686	0.2873	0.4274	0.9316	0.2997	0.4458	1.0020	0.2853	0.4248	0.9341
DINOv3 [45]+VGGT [56]	0.3068	0.4553	0.9909	0.3612	0.5315	1.1989	0.3833	0.5649	1.3307	0.3504	0.5172	1.1735
DINOv2† [34]+VGGT [56]	0.3068	0.4553	0.9906	0.3612	0.5314	1.1987	0.3833	0.5649	1.3304	0.3504	0.5172	1.1732
RobustVGGT-A	0.2732	0.4094	0.8719	0.2792	0.4153	0.8806	0.2930	0.4349	0.9310	0.2818	0.4199	0.8945
RobustVGGT-F	0.2641	0.3936	0.8420	0.2645	0.3949	0.8402	0.2664	0.3973	0.8388	0.2650	0.3953	0.8403
<b>On-the-Go</b>												
MASt3R-SfM [12]	0.0754	0.1548	2.0281	0.0749	0.1474	1.9934	0.0768	0.1510	2.0328	0.0757	0.15107	2.0181
VGGT [56]	0.0788	0.1239	1.0261	0.1281	0.1963	1.4194	0.1562	0.2393	1.7315	0.1210	0.1865	1.3923
MegaLoc [6]+VGGT [56]	0.0658	0.1056	0.9090	0.1044	0.1612	1.1516	0.1229	0.1881	1.3315	0.0977	0.1516	1.1307
MegaLoc* [6]+VGGT [56]	0.0529	0.0872	0.8366	0.0580	0.0942	0.8812	0.0637	0.1033	0.9464	0.0582	0.0949	0.8881
DINOv3 [45]+VGGT [56]	0.0675	0.1077	0.9184	0.1075	0.1667	1.2201	0.1312	0.2025	1.4602	0.1021	0.1589	1.1996
DINOv2† [34]+VGGT [56]	0.0788	0.1239	1.0261	0.1281	0.1963	1.4194	0.1562	0.2393	1.7315	0.1210	0.1865	1.3923
RobustVGGT-A	0.0578	0.0952	0.8800	0.0790	0.1253	1.2922	0.0697	0.1126	1.0361	0.0688	0.1110	1.0694
RobustVGGT-F	0.0521	0.0861	0.8179	0.0568	0.0931	0.8914	0.0660	0.1055	0.9872	0.0583	0.0949	0.8988
<b>RobustNeRF</b>												
MASt3R-SfM [12]	0.1153	0.2597	2.7124	0.1196	0.2650	2.7617	0.1182	0.2626	2.6882	0.1177	0.2624	2.7208
VGGT [56]	0.1519	0.2742	1.2052	0.1598	0.2908	1.2311	0.1680	0.3062	1.3493	0.1599	0.2904	1.2619
MegaLoc [6]+VGGT [56]	0.1496	0.2692	1.1920	0.1573	0.2847	1.2199	0.1618	0.2934	1.2721	0.1562	0.2824	1.2280
MegaLoc* [6]+VGGT [56]	0.1352	0.2418	1.1707	0.1358	0.2416	1.1663	0.1356	0.2394	1.1552	0.1355	0.2409	1.1641
DINOv3 [45]+VGGT [56]	0.1516	0.2738	1.2032	0.1595	0.2902	1.2296	0.1677	0.3055	1.3426	0.1596	0.2898	1.2585
DINOv2† [34]+VGGT [56]	0.1519	0.2742	1.2052	0.1598	0.2908	1.2311	0.1680	0.3062	1.3493	0.1599	0.2904	1.2619
RobustVGGT-A	0.1361	0.2433	1.1766	0.1379	0.2447	1.1657	0.1406	0.2478	1.1632	0.1382	0.2453	1.1685
RobustVGGT-F	0.1388	0.2480	1.1656	0.1374	0.2432	1.1670	0.1374	0.2415	1.1514	0.1379	0.2442	1.1613
<b>ETH3D</b>												
MASt3R-SfM [12]	2.3871	4.2586	77.368	2.3931	4.2766	78.521	2.3796	4.1958	76.4021	2.3866	4.2437	77.4303
VGGT [56]	0.8572	1.3675	6.3908	0.9182	1.5028	9.6272	1.0165	1.7348	15.2774	0.9306	1.5350	10.4318
MegaLoc [6]+VGGT [56]	0.9275	1.4470	5.5320	0.9233	1.4789	7.5607	0.9639	1.5977	11.4364	0.9382	1.5079	8.1764
MegaLoc* [6]+VGGT [56]	0.9170	1.4904	3.7593	0.9418	1.5194	4.3126	0.9800	1.5802	5.7108	0.9463	1.5300	4.5942
DINOv3 [45]+VGGT [56]	0.8551	1.3667	6.2305	0.9113	1.4891	9.4103	1.0027	1.7022	14.9265	0.9230	1.5193	10.1891
DINOv2† [34]+VGGT [56]	0.8556	1.3661	6.2515	0.9188	1.5022	9.5374	1.0165	1.7346	15.2582	0.9303	1.5343	10.3490
RobustVGGT-A	0.7447	1.1724	3.8938	0.7673	1.2123	3.7325	0.6874	1.0708	4.4779	0.7331	1.1518	4.0347
RobustVGGT-F	0.6224	1.0300	2.7304	0.8038	1.3159	2.9959	0.8636	1.3882	3.4866	0.7633	1.2447	3.0710

Table 2. **Multi-view depth estimation results.** Gray text indicates methods not directly comparable; they are included for reference only.

Methods	ETH3D							
	Small		Medium		Large		Avg	
	AbsRel ↓	$\delta < 1.25 \uparrow$	AbsRel ↓	$\delta < 1.25 \uparrow$	AbsRel ↓	$\delta < 1.25 \uparrow$	AbsRel ↓	$\delta < 1.25 \uparrow$
MASt3R-SfM [12]	0.0779	0.9329	0.0789	0.9321	0.0777	0.9327	0.0782	0.9326
VGGT [56]	0.0431	0.9683	0.0422	0.9730	0.0403	0.9776	0.0419	0.9730
MegaLoc [6]+VGGT [56]	0.0391	0.9729	0.0435	0.9694	0.0409	0.9759	0.0411	0.9727
MegaLoc* [6]+VGGT [56]	0.0291	0.9844	0.0318	0.9822	0.0365	0.9772	0.0325	0.9813
DINOv3 [45]+VGGT [56]	0.0430	0.9683	0.0422	0.9729	0.0399	0.9780	0.0417	0.9731
DINOv2† [34]+VGGT [56]	0.0431	0.9683	0.0422	0.9730	0.0403	0.9776	0.0419	0.9730
RobustVGGT-A	0.0308	0.9828	0.0313	0.9822	0.0351	0.9770	0.0324	0.9807
RobustVGGT-F	0.0288	0.9840	0.0297	0.9833	0.0319	0.9813	0.0301	0.9829

over 10 random trials per noise level.

Quantitative results are summarized in Tab. 1, with representative trajectories in Fig. 6. (i) *Baselines without explicit filtering.* VGGT shows a trend that performance degrades from *Small*→*Medium*→*Large* noise, with ATE and

RPE increasing as more distractors are introduced, reflecting the absence of a view-filtering mechanism. In contrast, ours shows more robust performance, without significant performance degradations. This trend is also shown in Fig. 10. (ii) *Pre-filtering baselines.* MegaLoc+VGGT,

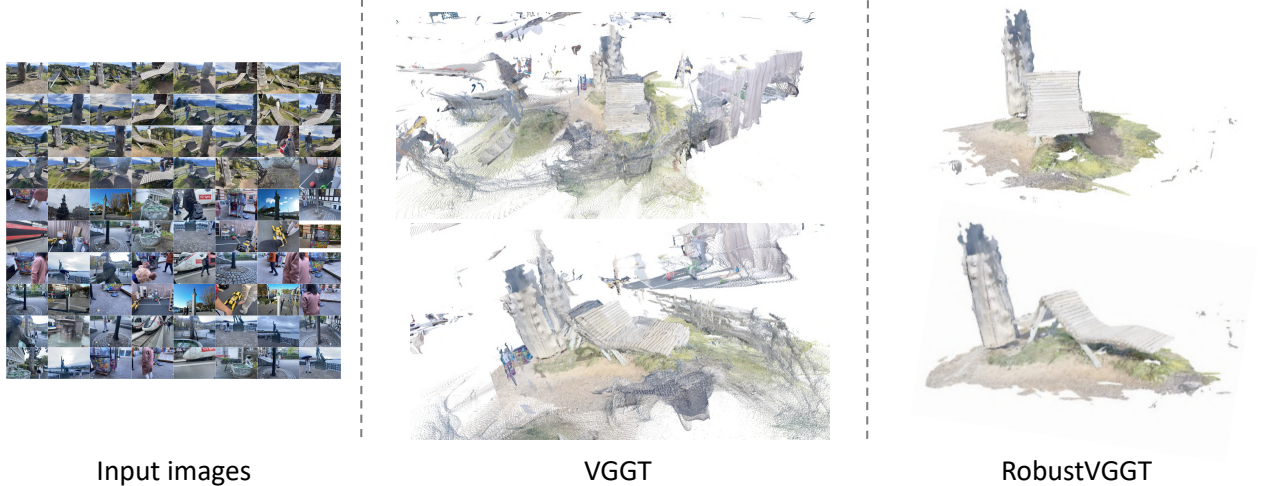


Figure 8. Visualization of point maps produced by VGGT and RobustVGGT- $\mathcal{F}$ .



Figure 9. Visualization of point maps produced by VGGT and RobustVGGT- $\mathcal{F}$  on internet-collected images.

DINOv3+VGGT, and DINO<sup>†</sup>+VGGT mitigate some errors but despite their dataset-specific hyperparameter tuning, which is determined by providing an oracle knowledge of the number of clean images, our method achieves the lowest errors using a *single global threshold*. Note that on Robust-NeRF, MAST3R-SfM achieves lower ATE than our method. We attribute this to the dataset’s small, highly overlapping scenes, where global view-graph optimization and bundle adjustment are particularly effective, diminishing the relative benefit of pre-filtering. (iii) *DINO-based variants*. Although DINO features are known for their strong generalization, our method yields larger gains across all noise levels, suggesting that strong descriptors alone are insufficient without geometry-aware selection.

**Multi-view depth estimation.** Following practice in affine-invariant depth estimation [27, 60], we align the predicted depth maps to the ground truth using a scale and shift, and evaluate performance using AbsRel, a mean absolute relative error, and  $\delta < 1.25$ , percentage of pixels whose predicted-to-GT depth ratio is within 1.25, on valid pixels after alignment of predicted and ground-truth depths. Tab. 2 shows the quantitative comparisons that exhibit the similar trend as for poses: methods without explicit view filtering, e.g., VGGT and MAST3R-SfM, tend to degrade from when

the distracting images are introduced. Pre-filtering baselines recover part of the loss but our variants, RobustVGGT- $\mathcal{A}$  and RobustVGGT- $\mathcal{F}$ , achieve the best results across all noise levels. We also observe apparent differences in visualized multi-view depth, as exemplified in Fig. 7. We also present the point map visualizations of VGGT and our method in Fig. 8 and Fig. 9. As can be seen from the chair example in Fig. 8, without noise filtering, the reconstruction for a clean image is noticeably degraded. In Fig. 9, we also show our robustness of reconstruction on internet-collected images.

### 4.3. Ablation studies and analysis

**Effects of varying threshold hyperparameter.** In this ablation study, we investigate the effects of varying the threshold value for  $\tau^O$ . We use Phototourism and On-the-Go datasets to validate both the generalizability and robustness of our approach. We include both of our variants, VGGT- $\mathcal{A}$  and VGGT- $\mathcal{F}$ . The results are summarized in Tab. 3. From the results, for RobustVGGT- $\mathcal{A}$ , the best camera estimation performance was achieved at  $\tau = 0.05$ , while for RobustVGGT- $\mathcal{F}$ , the optimal value was  $\tau = 0.65$ . These threshold values were therefore used for all evaluations.

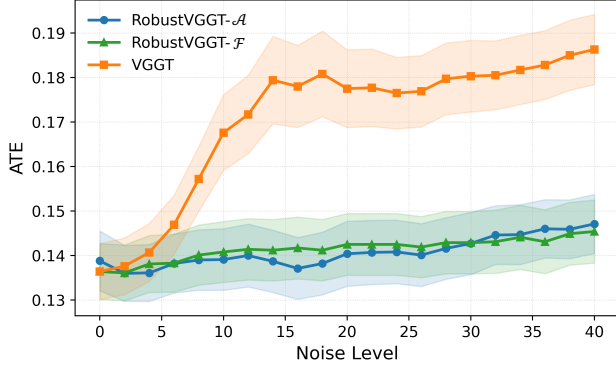


Figure 10. **Camera ATE vs. noise level.** VGGT without explicit view filtering degrade as the number of noisy views increases; Our approach enables robust 3D reconstruction.

Table 3. **Ablation study on varying threshold values  $\tau$ .** We report the results of (a) RobustVGGT-A and (b) RobustVGGT-F on Phototourism and On-the-Go using camera pose estimation metrics. Results are formatted as Phototourism / On-the-Go.

$\tau^{min}$	ATE	RPE <sub>cross</sub>	RPE <sub>out</sub>	$\tau^{out}$	ATE	RPE <sub>cross</sub>	RPE <sub>out</sub>
0.05	0.2818 / 0.0688	0.4199 / 0.1110	0.8945 / 1.0694	0.65	0.2650 / 0.0583	0.3953 / 0.0949	0.8403 / 0.8988
0.04	0.2968 / 0.0729	0.4403 / 0.1172	0.9419 / 1.0266	0.55	0.2748 / 0.0671	0.4088 / 0.1085	0.8584 / 1.1270
0.03	0.3130 / 0.1046	0.4632 / 0.1629	1.0174 / 1.4162	0.45	0.2870 / 0.0702	0.4254 / 0.1128	0.8966 / 0.8966
0.02	0.3418 / 0.1132	0.5039 / 0.1748	1.1306 / 1.2880	0.35	0.2777 / 0.0820	0.4114 / 0.1303	0.9708 / 1.2868

(a) RobustVGGT-A

(b) RobustVGGT-F

**Success rate of distractor rejection.** Tab. 4 shows that our method consistently rejects distractors more reliably than the baselines across datasets. For example, on On-the-Go and ETH3D, VGGT-F attains the highest average success and VGGT-A achieves the highest success rate on other datasets. We attribute this to VGGT’s *cross-view* reasoning, which provides stronger rejection signals than single-view global descriptors typical in VPR. Interestingly, DINOv3 performs poorly for distractor rejection: regardless of how we derive a global descriptor, *e.g.*, CLS token or GeM pooling [35], or whether we use local-token similarities, the success rate remains low. We attribute this to its appearance/semantics-driven training—features group visually similar images but are largely agnostic to geometric overlap—so non-overlapping yet look-alike distractors are not reliably filtered, and the model is not trained for view selection.

While this experiment mirrors common VPR benchmarking, it is noteworthy to mention that the scale of input image quantities is different: VGGT operates on tens to 100 images per batch, whereas VPR systems routinely handle thousands. Nevertheless, the approaches are complementary: VGGT-based view selection can re-rank or filter retrieval candidates, suggesting a practical route toward multi-view-aware place recognition at scale.

Table 4. **Success rate of distractor rejection across noise levels.**

Dataset	Noise level	MegaLoc [6]	MegaLoc* [6]	DINOv3 [45]	RobustVGGT-F	RobustVGGT-A
Phototourism	Small	0.517	0.653	0.000	0.783	0.907
	Medium	0.524	0.662	0.000	0.866	0.905
	Large	0.522	0.663	0.000	0.874	0.859
	Average	0.521	0.659	0.000	0.841	0.890
On-the-Go	Small	0.420	0.924	0.264	0.948	0.850
	Medium	0.429	0.923	0.257	0.940	0.902
	Large	0.427	0.922	0.261	0.921	0.899
	Average	0.425	0.923	0.261	0.936	0.884
RobustNeRF	Small	0.100	0.644	0.014	0.546	0.692
	Medium	0.100	0.647	0.015	0.602	0.626
	Large	0.112	0.650	0.014	0.610	0.606
	Average	0.104	0.647	0.014	0.586	0.641
ETH3D	Small	0.292	0.888	0.029	0.995	0.885
	Medium	0.298	0.891	0.034	0.987	0.926
	Large	0.303	0.883	0.040	0.974	0.930
	Average	0.298	0.887	0.034	0.985	0.914

## 5. Conclusion

In this work, we investigated robustness in feed-forward 3D reconstruction under noisy, in-the-wild image collections. Our analysis revealed an emergent noise-suppression behavior in modern feed-forward architecture *e.g.*, VGGT. We observe that internal attention and feature representations consistently emphasize spatially and geometrically consistent views while downweighting distractors. Building on this finding, we introduced a training-free view filtering mechanism that ranks and selects context images using a single global threshold. The approach is simple to deploy, complementary to existing pipelines, and generalizes datasets, yielding consistent improvements over retrieval-based baselines while preserving the efficiency advantages of feed-forward reconstruction.

## Acknowledgments

C.F. was supported in part through NSF grants 2514030 and 2238968 in this work. The visit of J.H. to NYU was through the NYU-KAIST collaboration program. This research was supported by the ETH AI Center through an ETH AI Center postdoctoral fellowship to Sunghwan Hong.

## Appendix

This supplementary material provides additional details and analyses to support the main paper, organized as follows:

- **Implementation details (§A):** Specific hyperparameters, experimental settings, and pseudo-code for reproducibility.
- **Additional Experiments (§B):** Generalization analysis on the Pi3 architecture and introduction of a variant of our method that combines RobustVGGT- $\mathcal{A}$  and VGGT- $\mathcal{F}$ .
- **Qualitative Results (§C):** Visual comparisons of 3D reconstructions and internal attention/feature map visualizations.
- **Limitations and Future Works (§E):** Discussion on current constraints and potential directions for explorations.

### A. Implementation Details

We build our method on top of VGGT. For VGGT- $\mathcal{A}$ , we set the attention threshold to  $\tau^{\text{attn}} = 0.05$ , and for VGGT- $\mathcal{F}$ , we set the feature threshold to  $\tau^{\text{feat}} = 0.65$ . The same thresholds are used for all benchmark datasets. Unless otherwise specified, all experiments are conducted on a single NVIDIA A6000 GPU paired with an AMD EPYC 7543 CPU. PyTorch-style pseudo-code for VGGT- $\mathcal{F}$  and VGGT- $\mathcal{A}$  is provided in Alg. 1 and Alg. 2, respectively.

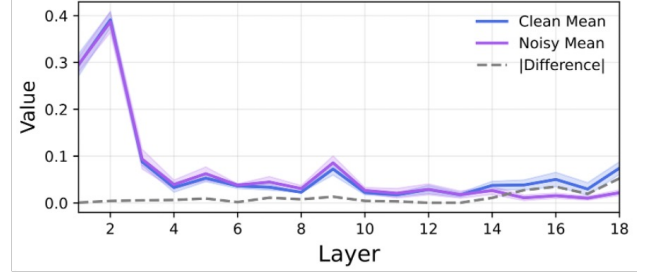
### B. Additional Experiments

**Analysis on Pi3.** In this section, we conduct an additional experiment using Pi3 [58], a preprint that shares a similar architecture as VGGT [56]. Following the procedure described in our main paper, we first perform a layer-wise analysis, measuring the gap between clean and distractor views in terms of attention and feature similarity. From Fig. 11, we observe a similar trend to VGGT: the gap steadily increases and peaks in the final layers. Among the layers, layer 17 exhibits the largest difference, and we therefore use this layer for view filtering.

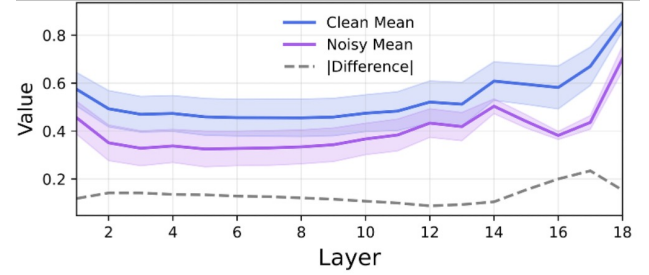
Based on this analysis, we evaluate the effectiveness of the internal representations at this layer. The results are summarized in Tab. 5 and Tab. 6. As the noise level increases, our method consistently proves beneficial for both camera pose estimation and multi-view depth estimation.

However, it is noteworthy that as shown in Tab. 7, the success rate of distractor rejection is relatively low. This may explain the smaller gap observed in Fig. 11 compared to the analysis on VGGT.

**Blending  $\tau^{\text{attn}}$  and  $\tau^{\text{feat}}$ .** We further introduce a variant of our method that combines RobustVGGT- $\mathcal{A}$  and RobustVGGT- $\mathcal{F}$ , integrating attention-based and feature-based rejection into a single score. This experiment is intended to provide insight into how a simple fusion of the



(a) Attention analysis



(b) Feature analysis

Figure 11. **Layer-wise analysis of Pi3 [58].** We measure the gap between clean and distractor views for attention and feature similarity across Pi3’s all layers. The separation grows with depth and peaks at the final layer, indicating emergent noise suppression.

two signals can improve view filtering and motivate more sophisticated variants.

The final score is obtained by first normalizing the attention scores from RobustVGGT- $\mathcal{A}$  and the cosine similarities from RobustVGGT- $\mathcal{F}$ , and then aggregating them with a weighted sum:

$$r_{i \rightarrow j}^{\text{agg}} = \alpha \bar{r}_{i \rightarrow j}^{\text{att}} + (1 - \alpha) \bar{r}_{i \rightarrow j}^{\text{feat}}, \quad \alpha \in [0, 1], \quad (5)$$

where  $\bar{r}$  denotes the normalized score. The context set for  $I_i$  is then defined as

$$\phi(i) = \{j \mid j = i \text{ or } r_{i \rightarrow j}^{\text{agg}} \geq \tau^{\text{agg}}\}, \quad (6)$$

with a single fixed threshold  $\tau^{\text{agg}}$  shared across all benchmarks. We set  $\alpha = 0.5$  and  $\tau^{\text{agg}} = 0.4$  in all experiments. As shown in Tab. 9, the combined approach yields more robust performance across all datasets. Furthermore, as can be seen in Tab. 8, the combined method also achieves better performance in terms of success rate.

### C. Additional Qualitative Results

We provide more qualitative results in Fig. 12, where we show a comparison of reconstructed scenes between our method and VGGT. As can be seen in the reconstructed point maps, VGGT—without filtering out distractor images—yields severely degraded reconstructions even for



views corresponding to clean images. Furthermore, as shown in Fig. 13, when reconstructing scenes using landmark images collected from the internet (e.g., Google) in real-world scenarios, VGGT fails to reject distracting or irrelevant images, resulting in inaccurate scene reconstructions. In contrast, our method robustly rejects such images and produces significantly more reliable scene reconstructions.

## D. Additional Visualizations

We also provide additional visualizations of attention maps, feature maps and correlation maps on Phototourism and ETH3D datasets, in Fig. 14, Fig. 15, Fig. 16, Fig. 17, Fig. 18 and Fig. 19. Interestingly, attention visualizations indicate that L23 allocates elevated attention to distractor images. Coupled with the observed suppression at L24, this is consistent with a two-stage behavior in the final layers: L23 exposes or aggregates signals from distractors, and L24 performs the actual rejection. While not proof of a hard specialization, this layer-wise pattern supports our hypothesis of late-layer differentiation between exposure and suppression.

## E. Limitations and Future Works

In this work, we showed that feed-forward 3D geometry foundation models *e.g.*, VGGT, exhibit an *emergent* noise-suppression behavior, which we exploit to build a simple, training-free, architecture-free view-selection module that is complementary to existing pipelines and effective across benchmarks. Our approach has several limitations and offers a few potential explorations: it operates at the *view* level and does not perform token/patch-wise filtering, which could further improve reconstruction but is beyond our current scope and leave it for a future work; it requires two forward passes (scoring then reconstruction), introducing a modest runtime overhead that remains substantially lower than retrieval-style prefiltering that evaluates per image *e.g.*, MegaLoc’s  $O(N)$  passes; and its throughput is bounded by the backbone’s batching capacity (typically tens to  $\sim 100$  images on an RTX A6000). These constraints can be mitigated with larger GPUs or lighter backbones, and scaled via hierarchical or cluster-wise filtering (e.g., applying our selector within VPR-formed clusters), offering a practical path to broader deployment without retraining.

Table 5. Camera pose estimation of Pi3.

Methods	Small			Medium			Large			Avg		
	ATE ↓	RPE <sub>trans</sub> ↓	RPE <sub>rot</sub> ↓	ATE ↓	RPE <sub>trans</sub> ↓	RPE <sub>rot</sub> ↓	ATE ↓	RPE <sub>trans</sub> ↓	RPE <sub>rot</sub> ↓	ATE ↓	RPE <sub>trans</sub> ↓	RPE <sub>rot</sub> ↓
<b>Phototourism</b>												
Pi3 [58]	0.2512	0.3815	0.9914	0.3861	0.6049	1.8208	0.5740	0.8962	3.1781	0.4038	0.6275	1.9968
RobustPi3- $\mathcal{A}$	0.2382	0.3606	0.9211	0.2652	0.4361	1.2007	0.3174	0.5730	2.6909	0.2736	0.4566	1.6042
RobustPi3- $\mathcal{F}$	0.2056	0.3084	0.8355	0.3093	0.4749	1.4506	0.4605	0.7110	2.5300	0.3251	0.4981	1.6054
<b>On-the-Go</b>												
Pi3 [58]	0.0860	0.1348	1.1495	0.1581	0.2454	1.8549	0.4234	0.6715	4.5146	0.2225	0.3506	2.5063
RobustPi3- $\mathcal{A}$	0.0718	0.1150	0.9588	0.0903	0.1441	1.0998	0.1506	0.2832	3.1712	0.1042	0.1808	1.7433
RobustPi3- $\mathcal{F}$	0.0575	0.0947	0.8910	0.0651	0.1050	0.9831	0.1736	0.2701	1.8804	0.0987	0.1566	1.2515
<b>RobustNeRF</b>												
Pi3 [58]	0.1467	0.2983	1.0091	0.2433	0.4555	3.4803	0.3204	0.5974	4.6081	0.2368	0.4504	3.0325
RobustPi3- $\mathcal{A}$	0.1484	0.3024	0.9915	0.2258	0.4689	3.0924	0.2258	0.4689	3.0924	0.2000	0.4134	2.3921
RobustPi3- $\mathcal{F}$	0.1515	0.3080	0.9906	0.1576	0.3151	1.0809	0.1813	0.3491	1.4606	0.1635	0.3241	1.1774
<b>ETH3D</b>												
Pi3 [58]	0.3533	0.5717	3.5348	0.5495	0.8535	6.2596	1.0319	1.6258	19.9132	0.6449	1.0170	9.9025
RobustPi3- $\mathcal{A}$	0.3275	0.5217	2.5944	0.4297	0.6718	3.8187	0.6779	1.0717	8.0849	0.4784	0.7551	4.8327
RobustPi3- $\mathcal{F}$	0.1954	0.3230	2.5088	0.2906	0.4810	3.7853	0.5922	0.9473	7.6219	0.3594	0.5838	4.6387

Table 6. Multi-view depth estimation results of Pi3.

Methods	ETH3D							
	Small		Medium		Large		Avg	
	AbsRel ↓	$\delta < 1.25 \uparrow$	AbsRel ↓	$\delta < 1.25 \uparrow$	AbsRel ↓	$\delta < 1.25 \uparrow$	AbsRel ↓	$\delta < 1.25 \uparrow$
Pi3 [58]	0.0215	0.9947	0.0255	0.9928	0.0306	0.9901	0.0258	0.9925
RobustPi3- $\mathcal{A}$	0.0208	0.9950	0.0233	0.9939	0.0259	0.9929	0.0233	0.9939
RobustPi3- $\mathcal{F}$	0.0188	0.9957	0.0204	0.9951	0.0254	0.9928	0.0215	0.9946

Table 7. Success rate of distractor rejection of Pi3 across noise levels.

Dataset	Noise level	RobustPi3- $\mathcal{F}$	RobustPi3- $\mathcal{A}$
Phototourism	Small	0.605	0.348
	Medium	0.408	0.558
	Large	0.285	0.670
	Average	0.433	0.525
On-the-Go	Small	0.919	0.323
	Medium	0.821	0.582
	Large	0.650	0.755
	Average	0.797	0.553
RobustNeRF	Small	0.662	0.366
	Medium	0.436	0.377
	Large	0.498	0.550
	Average	0.532	0.431
ETH3D	Small	0.938	0.198
	Medium	0.754	0.355
	Large	0.496	0.620
	Average	0.729	0.391

Table 8. Success rate of distractor rejection of VGGT across noise levels.

Dataset	Noise level	RobustVGGT- $\mathcal{F}$	RobustVGGT- $\mathcal{A}$	RobustVGGT- $\mathcal{A}$ + RobustVGGT- $\mathcal{F}$
Phototourism	Small	0.783	0.907	0.968
	Medium	0.866	0.905	0.982
	Large	0.874	0.859	0.983
	Average	0.841	0.890	0.978
On-the-Go	Small	0.948	0.850	0.966
	Medium	0.940	0.902	0.952
	Large	0.921	0.899	0.943
	Average	0.936	0.884	0.954
RobustNeRF	Small	0.546	0.692	0.734
	Medium	0.602	0.626	0.636
	Large	0.610	0.606	0.634
	Average	0.586	0.641	0.668
ETH3D	Small	0.995	0.885	0.997
	Medium	0.987	0.926	0.991
	Large	0.974	0.930	0.985
	Average	0.985	0.914	0.991

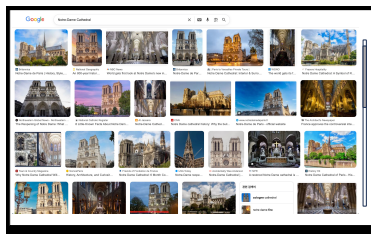
Table 9. **Camera pose estimation using the combination of RobustVGGT- $\mathcal{A}$  and RobustVGGT- $\mathcal{F}$ .** We report the camera pose evaluation for the RobustVGGT- $\mathcal{A} + F$  extension, which blends  $\tau^{\text{attn}}$  from RobustVGGT- $\mathcal{A}$  and  $\tau^{\text{feat}}$  from RobustVGGT- $\mathcal{F}$ .

Methods	Small			Medium			Large			Avg		
	ATE $\downarrow$	RPE <sub>trans</sub> $\downarrow$	RPE <sub>rot</sub> $\downarrow$	ATE $\downarrow$	RPE <sub>trans</sub> $\downarrow$	RPE <sub>rot</sub> $\downarrow$	ATE $\downarrow$	RPE <sub>trans</sub> $\downarrow$	RPE <sub>rot</sub> $\downarrow$	ATE $\downarrow$	RPE <sub>trans</sub> $\downarrow$	RPE <sub>rot</sub> $\downarrow$
<b>Phototourism</b>												
VGGT [56]	0.3068	0.4553	0.9906	0.3612	0.5314	1.1987	0.3833	0.5649	1.3304	0.3504	0.5172	1.1732
RobustVGGT- $\mathcal{A}$	0.2732	0.4094	0.8719	0.2792	0.4153	0.8806	0.2930	0.4349	0.9310	0.2818	0.4199	0.8945
RobustVGGT- $\mathcal{F}$	0.2641	0.3936	0.8420	0.2645	0.3949	0.8402	0.2664	0.3973	0.8388	0.2650	0.3953	0.8403
RobustVGGT- $\mathcal{A} + F$	0.2611	0.3895	0.8305	0.2610	0.3890	0.8289	0.2619	0.3904	0.8320	0.2613	0.3896	0.8305
<b>On-the-Go</b>												
VGGT [56]	0.0788	0.1239	1.0261	0.1281	0.1963	1.4194	0.1562	0.2393	1.7315	0.1210	0.1865	1.3923
RobustVGGT- $\mathcal{A}$	0.0578	0.0952	0.8800	0.0790	0.1253	1.2922	0.0697	0.1126	1.0361	0.0688	0.1110	1.0694
RobustVGGT- $\mathcal{F}$	0.0521	0.0861	0.8179	0.0568	0.0931	0.8914	0.0660	0.1055	0.9872	0.0583	0.0949	0.8988
RobustVGGT- $\mathcal{A} + F$	0.0519	0.0858	0.8146	0.0566	0.0924	0.8793	0.0614	0.0993	0.9550	0.0566	0.0925	0.8830
<b>RobustNeRF</b>												
VGGT [56]	0.1519	0.2742	1.2052	0.1598	0.2908	1.2311	0.1680	0.3062	1.3493	0.1599	0.2904	1.2619
RobustVGGT- $\mathcal{A}$	0.1361	0.2433	1.1766	0.1379	0.2447	1.1657	0.1406	0.2478	1.1632	0.1382	0.2453	1.1685
RobustVGGT- $\mathcal{F}$	0.1388	0.2480	1.1656	0.1374	0.2432	1.1670	0.1374	0.2415	1.1514	0.1379	0.2442	1.1613
RobustVGGT- $\mathcal{A} + F$	0.1361	0.2435	1.1783	0.1363	0.2413	1.1664	0.1365	0.2397	1.1577	0.1363	0.2415	1.1675
<b>ETH3D</b>												
VGGT [56]	0.8572	1.3675	6.3908	0.9182	1.5028	9.6272	1.0165	1.7348	15.2774	0.9306	1.5350	10.4318
RobustVGGT- $\mathcal{A}$	0.7447	1.1724	3.8938	0.7673	1.2123	3.7325	0.6874	1.0708	4.4779	0.7331	1.1518	4.0347
RobustVGGT- $\mathcal{F}$	0.6224	1.0300	2.7304	0.8038	1.3159	2.9959	0.8636	1.3882	3.4866	0.7633	1.2447	3.0710
RobustVGGT- $\mathcal{A} + F$	0.6521	1.0729	2.7305	0.7847	1.2671	3.1248	0.7861	1.2534	3.2919	0.7410	1.1978	3.0491

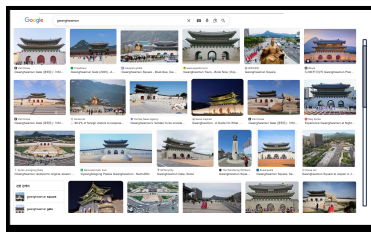


Figure 12. Visualization of point maps produced by VGGT and RobustVGGT on various datasets.

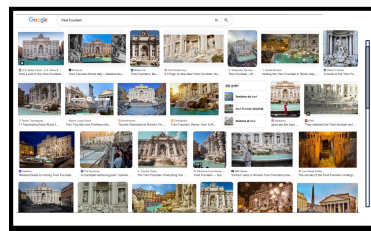
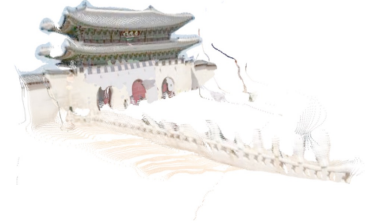




Q | Notre-Dame Cathedral



Q | Gwanghwamun



Q | Trevi Fountain



VGGT



RobustVGGT

Figure 13. Visualization of point maps produced by VGGT and RobustVGGT on internet-collected images.

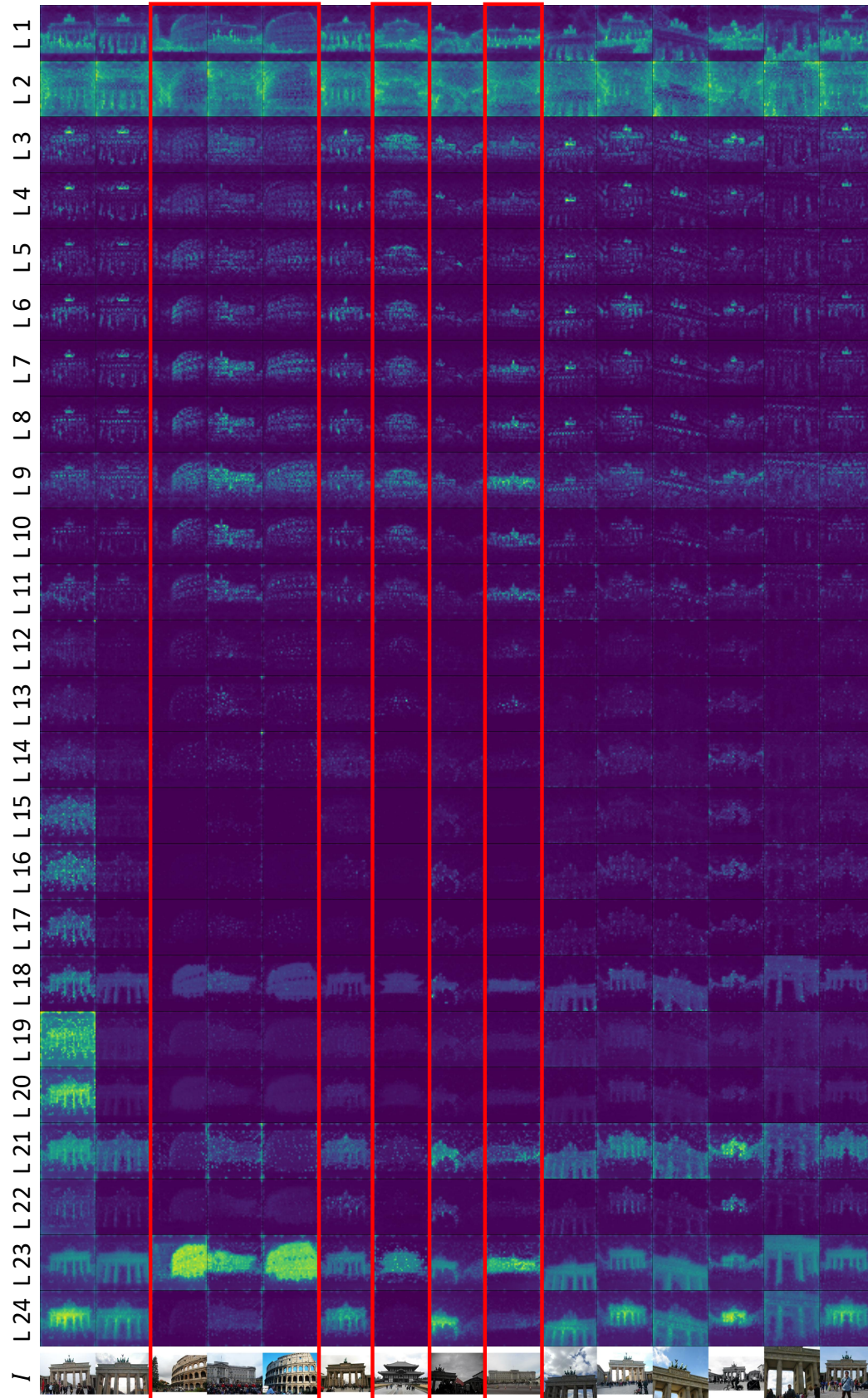


Figure 14. Visualization of attention maps across all layers of VGGT on the Phototourism dataset.



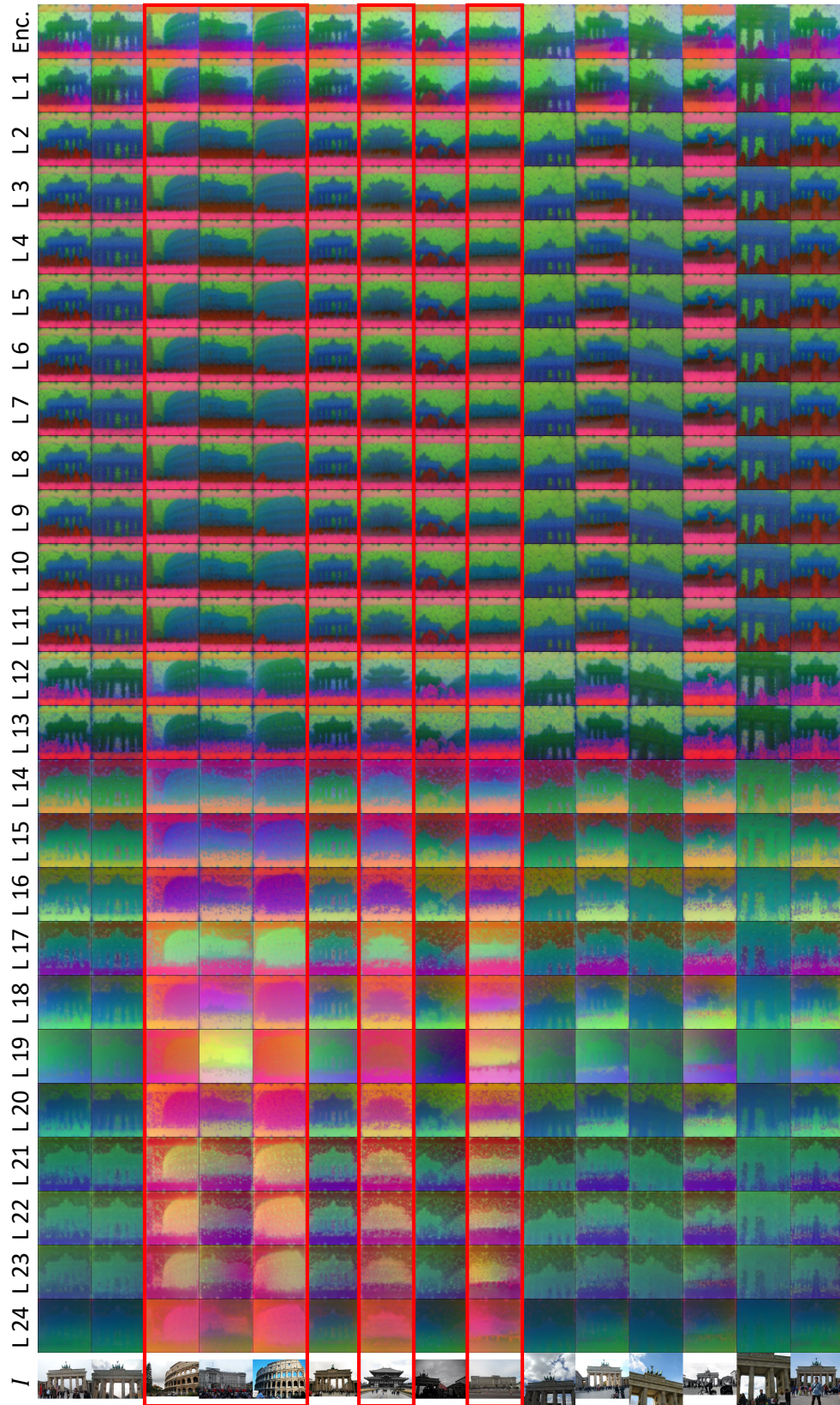


Figure 15. **Visualization of feature maps of all layers inside VGGT on Phototourism dataset.** *Enc.* denotes features from VGGT’s encoder.



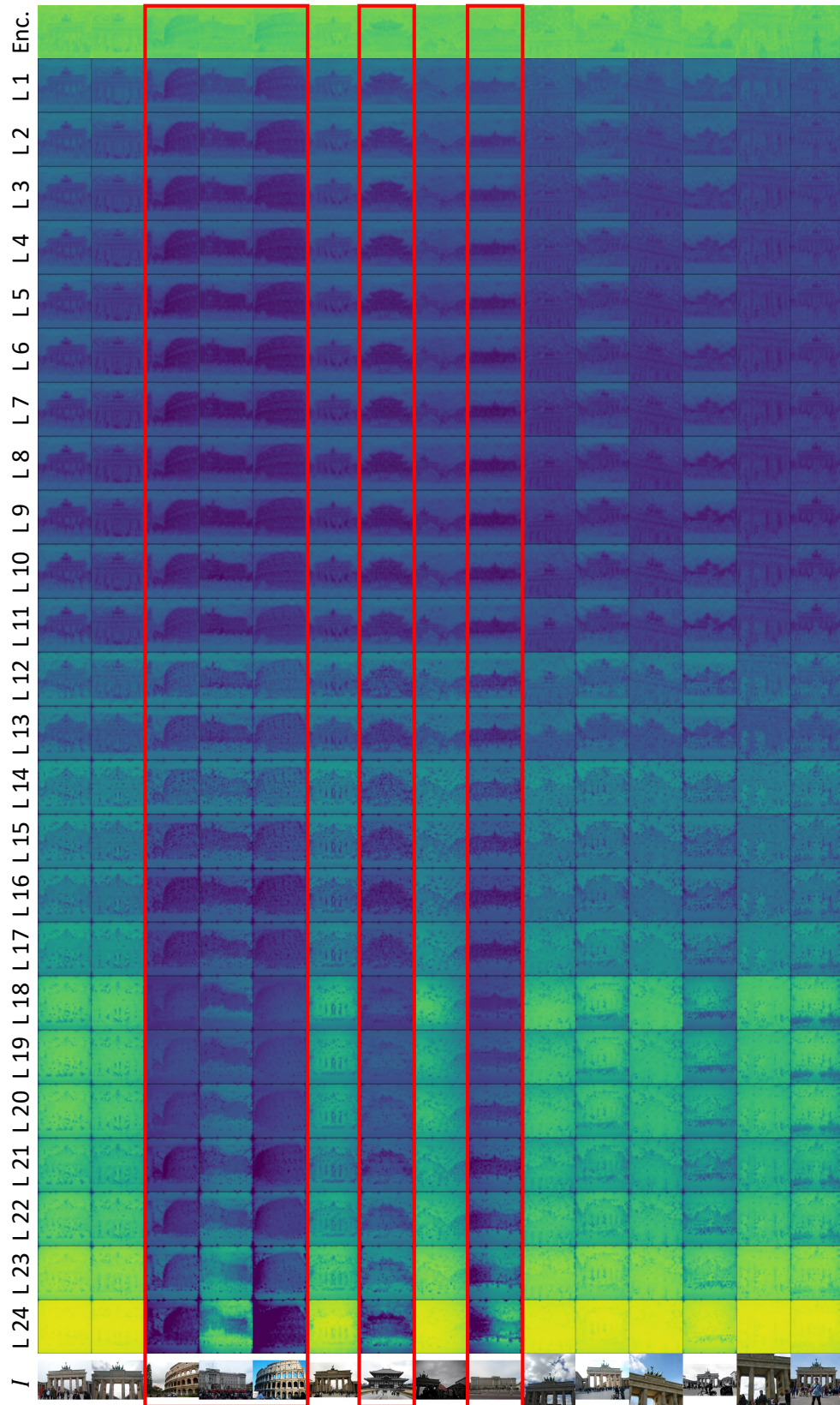


Figure 16. **Visualization of correlation maps across all layers of VGGT on the Phototourism dataset.** *Enc.* denotes features from VGGT’s encoder.



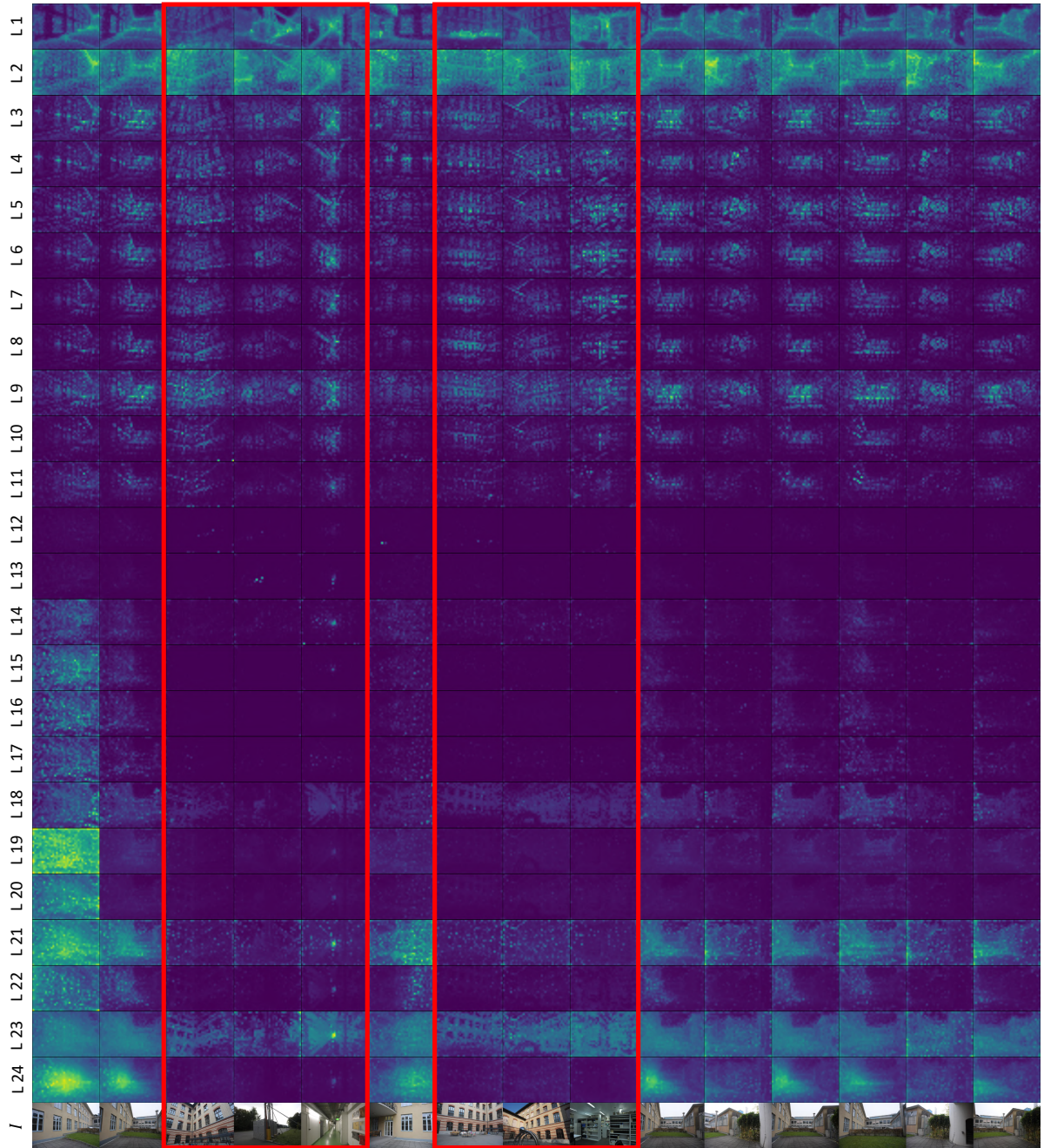


Figure 17. Visualization of attention maps across all VGGT layers on the ETH3D dataset.

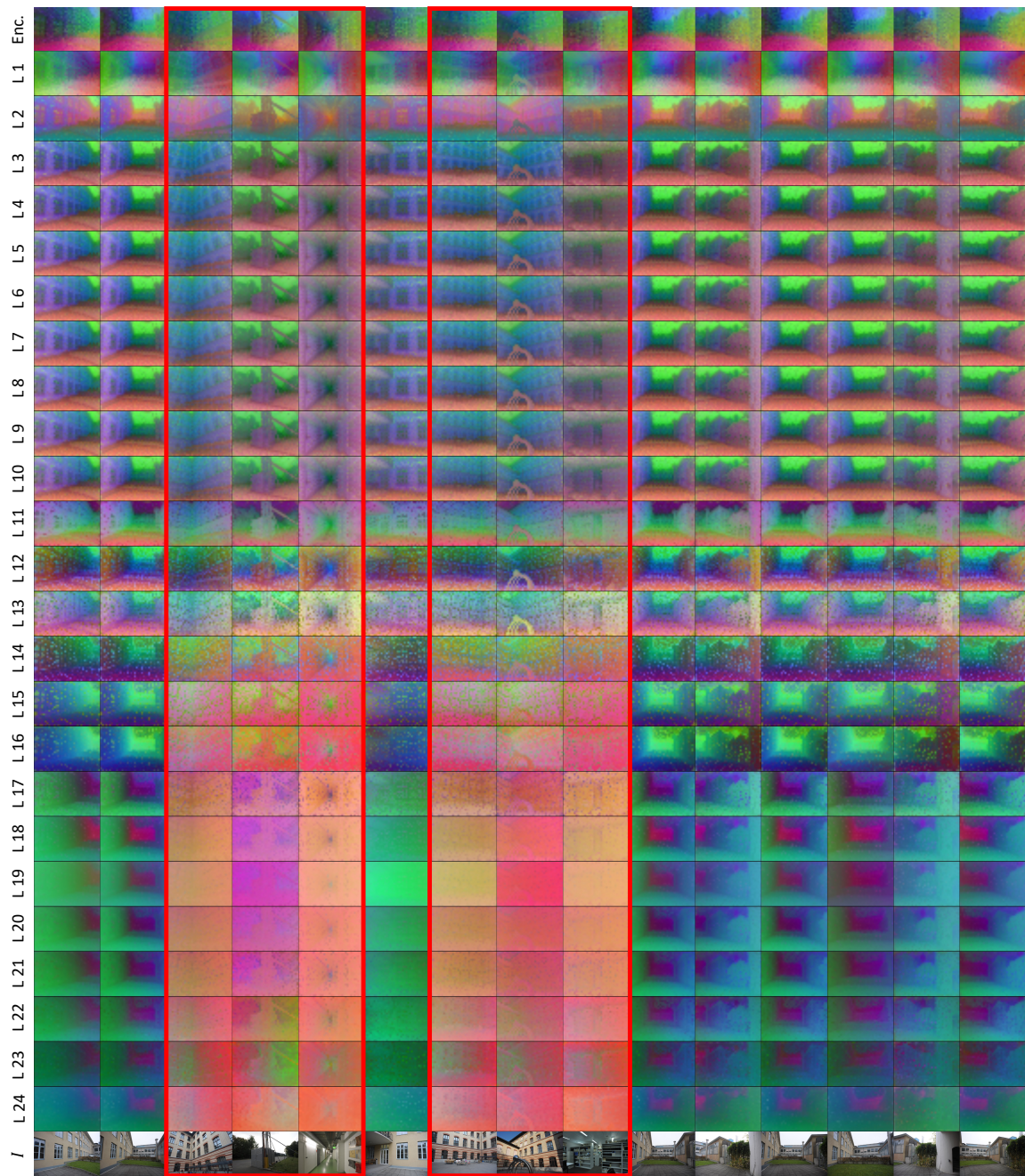


Figure 18. **Visualization of feature maps across all VGGT layers on the ETH3D dataset.** *Enc.* denotes features from VGGT’s encoder.



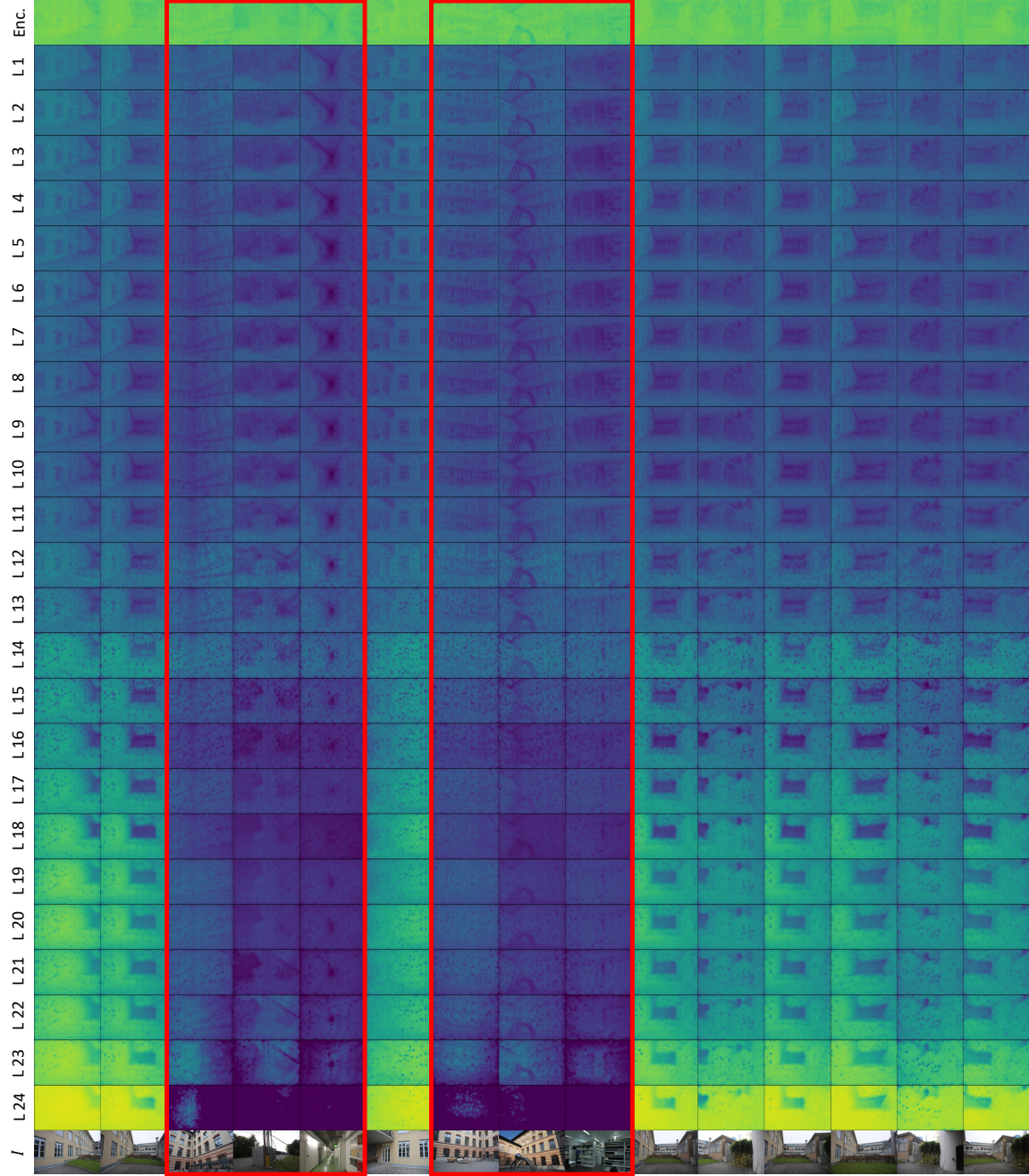


Figure 19. **Visualization of correlation maps across all VGGT layers on the ETH3D dataset.** *Enc.* denotes features from VGGT’s encoder.

---

**Algorithm 1** Pseudo-Code of RobustVGGT- $\mathcal{F}$ , PyTorch-like

---

```
1 class VGGT_F:
2     def forward(images, image_hw):
3         predictions, aggregated_tokens_list = VGGT(images)
4
5         target_layer = 23
6         aggregated_tokens_selected = aggregated_tokens_list[target_layer]
7         feature = aggregated_tokens_selected[..., 1024:]
8
9         H, W = image_hw
10        h_patches = H // patch_size
11        w_patches = W // patch_size
12        num_patch_tokens = h_patches * w_patches
13
14        feature = feature[:, :, patch_start_idx:, :] # (B, N, T, C)
15        B, N, T, C = feature.shape
16        layer_feat = feature.reshape(B * N, T, C)
17
18        ref_feat = layer_feat[0:1]
19        ref_feat_norm = normalize(ref_feat)
20        layer_feat_norm = normalize(layer_feat)
21
22        cos_sim = einsum(layer_feat_norm, ref_feat_norm) # (B*N, T, T)
23        cos_sim_mean = cos_sim.mean(-1).mean(-1) # (B*N,)
24
25        filtered_images = filter(images, cos_sim_mean, threshold=0.65)
26        predictions, _ = VGGT(filtered_images)
27
28    return predictions
```

---



---

**Algorithm 2** Pseudo-Code of RobustVGGT- $\mathcal{A}$ , PyTorch-like

---

```
1 class VGGT_A:
2     def forward(images, image_hw):
3         predictions, Q_layers, K_layers = VGGT(images)
4
5         H, W = image_hw
6         h_patches = H // patch_size
7         w_patches = W // patch_size
8         num_patch_tokens = h_patches * w_patches
9
10        Q = Q_layers[23]                # (B, H, T, D)
11        K = K_layers[23]                # (B, H, T, D)
12        T = int(K.shape[-2])
13        num_images_in_seq = T // tokens_per_image
14
15        q_first = Q[:, :, first_image_patch_start:first_image_patch_end, :]
16        Tk = int(num_images_in_seq * tokens_per_image)
17        K_slice = K[:, :, :Tk, :]
18        scale = 1.0 / sqrt(dim(q_first))
19        logits = einsum(q_first, K_slice) * scale    # (B, H, Nq, Tk)
20        probs = softmax(logits, dim=-1)
21        attn_first = probs.mean(dim=1).mean(dim=1)[0] # (Tk,)
22
23        maps_2d = []
24        for img_idx in range(num_images_in_seq):
25            start = img_idx * tokens_per_image + patch_start_idx
26            end = start + num_patch_tokens
27            if start >= len(attn_first):
28                break
29
30            patch_attn = attn_first[start:end]
31            attn2d = patch_attn.view(h_patches, w_patches)
32            maps_2d.append(attn2d)
33
34        global_norm = global_norm(maps_2d)
35        global_mean_val = float(global_norm.mean())
36
37        filtered_images = filter(images, global_mean_val, threshold=0.05)
38        predictions, _, _ = VGGT(filtered_images)
39
40        return predictions
```

---

## References

- [1] Sameer Agarwal, Yasutaka Furukawa, Noah Snavely, Ian Simon, Brian Curless, Steven M Seitz, and Richard Szeliski. Building rome in a day. *Communications of the ACM*, 54(10):105–112, 2011. 2
- [2] Honggyu An, Jin Hyeon Kim, Seonghoon Park, Jaewoo Jung, Jisang Han, Sunghwan Hong, and Seungryong Kim. Cross-view completion models are zero-shot correspondence estimators. In *Proceedings of the Computer Vision and Pattern Recognition Conference*, pages 1103–1115, 2025. 2
- [3] Relja Arandjelovic, Petr Gronat, Akihiko Torii, Tomas Pajdla, and Josef Sivic. Netvlad: Cnn architecture for weakly supervised place recognition. In *Proceedings of the IEEE conference on computer vision and pattern recognition*, pages 5297–5307, 2016. 2, 3
- [4] Daniel Barath, Jiri Matas, and Jana Noskova. Magsac: marginalizing sample consensus. In *Proceedings of the IEEE/CVF conference on computer vision and pattern recognition*, pages 10197–10205, 2019. 2
- [5] Daniel Barath, Jana Noskova, Maksym Ivashechkin, and Jiri Matas. Magsac++, a fast, reliable and accurate robust estimator. In *Proceedings of the IEEE/CVF conference on computer vision and pattern recognition*, pages 1304–1312, 2020. 2
- [6] Gabriele Berton and Carlo Masone. Megaloc: One retrieval to place them all. In *Proceedings of the Computer Vision and Pattern Recognition Conference*, pages 2861–2867, 2025. 2, 6, 7, 9
- [7] Eric Brachmann, Alexander Krull, Sebastian Nowozin, Jamie Shotton, Frank Michel, Stefan Gumhold, and Carsten Rother. Dsac-differentiable ransac for camera localization. In *Proceedings of the IEEE conference on computer vision and pattern recognition*, pages 6684–6692, 2017. 2
- [8] Seokju Cho, Sunghwan Hong, Sangryul Jeon, Yunsung Lee, Kwanghoon Sohn, and Seungryong Kim. Cats: Cost aggregation transformers for visual correspondence. *Advances in Neural Information Processing Systems*, 34:9011–9023, 2021. 2
- [9] Seokju Cho, Sunghwan Hong, and Seungryong Kim. Cats++: Boosting cost aggregation with convolutions and transformers. *IEEE Transactions on Pattern Analysis and Machine Intelligence*, 45(6):7174–7194, 2022. 2
- [10] Seokju Cho, Heeseong Shin, Sunghwan Hong, Anurag Arnab, Paul Hongsuck Seo, and Seungryong Kim. Catseg: Cost aggregation for open-vocabulary semantic segmentation. In *Proceedings of the IEEE/CVF Conference on Computer Vision and Pattern Recognition*, pages 4113–4123, 2024. 1
- [11] Daniel DeTone, Tomasz Malisiewicz, and Andrew Rabinovich. Superpoint: Self-supervised interest point detection and description. In *Proceedings of the IEEE conference on computer vision and pattern recognition workshops*, pages 224–236, 2018. 2
- [12] Bardienus Pieter Duisterhof, Lojze Zust, Philippe Weinzaepfel, Vincent Leroy, Yohann Cabon, and Jerome Revaud. Mast3r-sfm: a fully-integrated solution for unconstrained structure-from-motion. In *2025 International Conference on 3D Vision (3DV)*, pages 1–10. IEEE, 2025. 6, 7
- [13] Mihai Dusmanu, Ignacio Rocco, Tomas Pajdla, Marc Pollefeys, Josef Sivic, Akihiko Torii, and Torsten Sattler. D2-net: A trainable cnn for joint detection and description of local features. *arXiv preprint arXiv:1905.03561*, 2019. 2
- [14] Johan Edstedt, Qiyu Sun, Georg Bökman, Mårten Wadenbäck, and Michael Felsberg. Roma: Robust dense feature matching. In *Proceedings of the IEEE/CVF Conference on Computer Vision and Pattern Recognition*, pages 19790–19800, 2024. 2
- [15] Martin A Fischler and Robert C Bolles. Random sample consensus: a paradigm for model fitting with applications to image analysis and automated cartography. *Communications of the ACM*, 24(6):381–395, 1981. 1, 2
- [16] Xiaodong Gu, Zhiwen Fan, Siyu Zhu, Zuozhuo Dai, Feitong Tan, and Ping Tan. Cascade cost volume for high-resolution multi-view stereo and stereo matching. In *Proceedings of the IEEE/CVF conference on computer vision and pattern recognition*, pages 2495–2504, 2020. 2
- [17] Jisang Han, Honggyu An, Jaewoo Jung, Takuya Narihira, Junyoung Seo, Kazumi Fukuda, Chaehyun Kim, Sunghwan Hong, Yuki Mitsufuji, and Seungryong Kim. D<sup>2</sup> 2ust3r: Enhancing 3d reconstruction with 4d pointmaps for dynamic scenes. *arXiv preprint arXiv:2504.06264*, 2025. 2
- [18] Richard Hartley. *Multiple view geometry in computer vision*. Cambridge university press, 2003. 1, 2
- [19] Richard I Hartley and Peter Sturm. Triangulation. *Computer vision and image understanding*, 68(2):146–157, 1997. 2
- [20] Sunghwan Hong and Seungryong Kim. Deep matching prior: Test-time optimization for dense correspondence. In *Proceedings of the IEEE/CVF international conference on computer vision*, pages 9907–9917, 2021. 2
- [21] Sunghwan Hong, Jisu Nam, Seokju Cho, Susung Hong, Sangryul Jeon, Dongbo Min, and Seungryong Kim. Neural matching fields: Implicit representation of matching fields for visual correspondence. *Advances in Neural Information Processing Systems*, 35:13512–13526, 2022.
- [22] Sunghwan Hong, Seokju Cho, Seungryong Kim, and Stephen Lin. Unifying feature and cost aggregation with transformers for semantic and visual correspondence. *arXiv preprint arXiv:2403.11120*, 2024. 2
- [23] Sunghwan Hong, Jaewoo Jung, Heeseong Shin, Jisang Han, Jiaolong Yang, Chong Luo, and Seungryong Kim. Pf3plat: Pose-free feed-forward 3d gaussian splatting. *arXiv preprint arXiv:2410.22128*, 2024. 2
- [24] Sunghwan Hong, Jaewoo Jung, Heeseong Shin, Jiaolong Yang, Seungryong Kim, and Chong Luo. Unifying correspondence pose and nerf for generalized pose-free novel view synthesis. In *Proceedings of the IEEE/CVF Conference on Computer Vision and Pattern Recognition*, pages 20196–20206, 2024. 2
- [25] Hervé Jégou, Matthijs Douze, Cordelia Schmid, and Patrick Pérez. Aggregating local descriptors into a compact image representation. In *2010 IEEE computer society conference on computer vision and pattern recognition*, pages 3304–3311. IEEE, 2010. 2
- [26] Yuhe Jin, Dmytro Mishkin, Anastasiia Mishchuk, Jiri Matas, Pascal Fua, Kwang Moo Yi, and Eduard Trulls. Image

- matching across wide baselines: From paper to practice. *International Journal of Computer Vision*, 129(2):517–547, 2021. 5
- [27] Bingxin Ke, Anton Obukhov, Shengyu Huang, Nando Metzger, Rodrigo Caye Daudt, and Konrad Schindler. Repurposing diffusion-based image generators for monocular depth estimation. In *Proceedings of the IEEE/CVF conference on computer vision and pattern recognition*, pages 9492–9502, 2024. 8
- [28] Chaehyun Kim, Heeseong Shin, Eunbeen Hong, Heeji Yoon, Anurag Arnab, Paul Hongsuck Seo, Sunghwan Hong, and Seungryong Kim. Seg4diff: Unveiling open-vocabulary segmentation in text-to-image diffusion transformers. *arXiv preprint arXiv:2509.18096*, 2025. 1
- [29] JoungBin Lee, Jaewoo Jung, Jisang Han, Takuya Narihira, Kazumi Fukuda, Junyoung Seo, Sunghwan Hong, Yuki Mitsufuji, and Seungryong Kim. 3d scene prompting for scene-consistent camera-controllable video generation. *arXiv preprint arXiv:2510.14945*, 2025. 1
- [30] Vincent Leroy, Yohann Cabon, and Jérôme Revaud. Grounding image matching in 3d with mast3r. In *European Conference on Computer Vision*, pages 71–91. Springer, 2024. 1, 2, 3
- [31] David G Lowe. Distinctive image features from scale-invariant keypoints. *International journal of computer vision*, 60:91–110, 2004. 2
- [32] David Nister and Henrik Stewenius. Scalable recognition with a vocabulary tree. In *2006 IEEE Computer Society Conference on Computer Vision and Pattern Recognition (CVPR’06)*, pages 2161–2168. Ieee, 2006. 2
- [33] Hyeonwoo Noh, Andre Araujo, Jack Sim, Tobias Weyand, and Bohyung Han. Large-scale image retrieval with attentive deep local features. In *Proceedings of the IEEE international conference on computer vision*, pages 3456–3465, 2017. 2
- [34] Maxime Oquab, Timothée Darcet, Théo Moutakanni, Huy Vo, Marc Szafraniec, Vasil Khalidov, Pierre Fernandez, Daniel Haziza, Francisco Massa, Alaaeldin El-Nouby, et al. Dinov2: Learning robust visual features without supervision. *arXiv preprint arXiv:2304.07193*, 2023. 6, 7
- [35] Filip Radenović, Giorgos Tolias, and Ondřej Chum. Fine-tuning cnn image retrieval with no human annotation. *IEEE transactions on pattern analysis and machine intelligence*, 41(7):1655–1668, 2018. 2, 9
- [36] Weining Ren, Zihan Zhu, Boyang Sun, Jiaqi Chen, Marc Pollefeys, and Songyou Peng. Nerf on-the-go: Exploiting uncertainty for distractor-free nerfs in the wild. In *Proceedings of the IEEE/CVF Conference on Computer Vision and Pattern Recognition*, pages 8931–8940, 2024. 2, 5
- [37] Ignacio Rocco, Relja Arandjelovic, and Josef Sivic. Convolutional neural network architecture for geometric matching. In *Proceedings of the IEEE conference on computer vision and pattern recognition*, pages 6148–6157, 2017. 5
- [38] Ethan Rublee, Vincent Rabaud, Kurt Konolige, and Gary Bradski. Orb: An efficient alternative to sift or surf. In *2011 International conference on computer vision*, pages 2564–2571. Ieee, 2011. 1, 2
- [39] Sara Sabour, Suhani Vora, Daniel Duckworth, Ivan Krasin, David J Fleet, and Andrea Tagliasacchi. Robustnerf: Ignoring distractors with robust losses. In *Proceedings of the IEEE/CVF conference on computer vision and pattern recognition*, pages 20626–20636, 2023. 2, 6
- [40] Paul-Edouard Sarlin, Daniel DeTone, Tomasz Malisiewicz, and Andrew Rabinovich. Superglue: Learning feature matching with graph neural networks. In *Proceedings of the IEEE/CVF conference on computer vision and pattern recognition*, pages 4938–4947, 2020. 2
- [41] Johannes L Schonberger and Jan-Michael Frahm. Structure-from-motion revisited. In *Proceedings of the IEEE conference on computer vision and pattern recognition*, pages 4104–4113, 2016. 1, 2, 3
- [42] Thomas Schöps, Johannes L. Schönberger, Silvano Galliani, Torsten Sattler, Konrad Schindler, Marc Pollefeys, and Andreas Geiger. A multi-view stereo benchmark with high-resolution images and multi-camera videos. In *Conference on Computer Vision and Pattern Recognition (CVPR)*, 2017. 2
- [43] Thomas Schops, Johannes L Schonberger, Silvano Galliani, Torsten Sattler, Konrad Schindler, Marc Pollefeys, and Andreas Geiger. A multi-view stereo benchmark with high-resolution images and multi-camera videos. In *Proceedings of the IEEE conference on computer vision and pattern recognition*, pages 3260–3269, 2017. 6
- [44] Heeseong Shin, Chaehyun Kim, Sunghwan Hong, Seokju Cho, Anurag Arnab, Paul Hongsuck Seo, and Seungryong Kim. Towards open-vocabulary semantic segmentation without semantic labels. *Advances in Neural Information Processing Systems*, 37:9153–9177, 2024. 1
- [45] Oriane Siméoni, Huy V Vo, Maximilian Seitzer, Federico Baldassarre, Maxime Oquab, Cijo Jose, Vasil Khalidov, Marc Szafraniec, Seungeun Yi, Michaël Ramamonjisoa, et al. Dinov3. *arXiv preprint arXiv:2508.10104*, 2025. 6, 7, 9
- [46] Sivic and Zisserman. Video google: A text retrieval approach to object matching in videos. In *Proceedings ninth IEEE international conference on computer vision*, pages 1470–1477. IEEE, 2003. 2
- [47] Noah Snavely, Steven M Seitz, and Richard Szeliski. Photo tourism: exploring photo collections in 3d. In *ACM siggraph 2006 papers*, pages 835–846. 2006. 2
- [48] Noah Snavely, Steven M Seitz, and Richard Szeliski. Modeling the world from internet photo collections. *International journal of computer vision*, 80(2):189–210, 2008. 2
- [49] Jiaming Sun, Zehong Shen, Yuang Wang, Hujun Bao, and Xiaowei Zhou. Loftr: Detector-free local feature matching with transformers. In *Proceedings of the IEEE/CVF conference on computer vision and pattern recognition*, pages 8922–8931, 2021. 2
- [50] Chengzhou Tang and Ping Tan. Ba-net: Dense bundle adjustment network. *arXiv preprint arXiv:1806.04807*, 2018. 2
- [51] Zachary Teed and Jia Deng. Deepv2d: Video to depth with differentiable structure from motion. *arXiv preprint arXiv:1812.04605*, 2018. 2

- [52] Engin Tola, Vincent Lepetit, and Pascal Fua. A fast local descriptor for dense matching. In *2008 IEEE conference on computer vision and pattern recognition*, pages 1–8. IEEE, 2008. [2](#)
- [53] Bill Triggs, Philip F McLauchlan, Richard I Hartley, and Andrew W Fitzgibbon. Bundle adjustment—a modern synthesis. In *International workshop on vision algorithms*, pages 298–372. Springer, 1999. [1](#), [2](#)
- [54] Fangjinhua Wang, Silvano Galliani, Christoph Vogel, Pablo Speciale, and Marc Pollefeys. Patchmatchnet: Learned multi-view patchmatch stereo. In *Proceedings of the IEEE/CVF conference on computer vision and pattern recognition*, pages 14194–14203, 2021. [2](#)
- [55] Jianyuan Wang, Nikita Karaev, Christian Rupprecht, and David Novotny. Vggsfm: Visual geometry grounded deep structure from motion. In *Proceedings of the IEEE/CVF conference on computer vision and pattern recognition*, pages 21686–21697, 2024. [1](#)
- [56] Jianyuan Wang, Minghao Chen, Nikita Karaev, Andrea Vedaldi, Christian Rupprecht, and David Novotny. Vggt: Visual geometry grounded transformer. In *Proceedings of the Computer Vision and Pattern Recognition Conference*, pages 5294–5306, 2025. [1](#), [2](#), [3](#), [4](#), [5](#), [6](#), [7](#)
- [57] Shuzhe Wang, Vincent Leroy, Yohann Cabon, Boris Chidlovskii, and Jerome Revaud. Dust3r: Geometric 3d vision made easy. In *Proceedings of the IEEE/CVF Conference on Computer Vision and Pattern Recognition*, pages 20697–20709, 2024. [1](#), [2](#), [3](#)
- [58] Yifan Wang, Jianjun Zhou, Haoyi Zhu, Wenzheng Chang, Yang Zhou, Zizun Li, Junyi Chen, Jiangmiao Pang, Chunhua Shen, and Tong He.  $\pi^3$ : Permutation-equivariant visual geometry learning. *arXiv preprint arXiv:2507.13347*, 2025. [1](#), [3](#)
- [59] Tong Wei, Yash Patel, Alexander Shekhovtsov, Jiri Matas, and Daniel Barath. Generalized differentiable ransac. In *Proceedings of the IEEE/CVF International Conference on Computer Vision*, pages 17649–17660, 2023. [2](#)
- [60] Lihe Yang, Bingyi Kang, Zilong Huang, Xiaogang Xu, Jiashi Feng, and Hengshuang Zhao. Depth anything: Unleashing the power of large-scale unlabeled data. In *Proceedings of the IEEE/CVF conference on computer vision and pattern recognition*, pages 10371–10381, 2024. [8](#)
- [61] Yao Yao, Zixin Luo, Shiwei Li, Tian Fang, and Long Quan. Mvsnet: Depth inference for unstructured multi-view stereo. In *Proceedings of the European conference on computer vision (ECCV)*, pages 767–783, 2018. [2](#)
- [62] Yao Yao, Zixin Luo, Shiwei Li, Tianwei Shen, Tian Fang, and Long Quan. Recurrent mvsnet for high-resolution multi-view stereo depth inference. In *Proceedings of the IEEE/CVF conference on computer vision and pattern recognition*, pages 5525–5534, 2019. [2](#)
- [63] Heeji Yoon, Jaewoo Jung, Junwan Kim, Hyungyu Choi, Heeseong Shin, Sangbeom Lim, Honggyu An, Chaehyun Kim, Jisang Han, Donghyun Kim, et al. Visual representation alignment for multimodal large language models. *arXiv preprint arXiv:2509.07979*, 2025. [1](#)
- [64] Chenming Zhu, Tai Wang, Wenwei Zhang, Jiangmiao Pang, and Xihui Liu. Llava-3d: A simple yet effective pathway to empowering llms with 3d-awareness. *arXiv preprint arXiv:2409.18125*, 2024. [1](#)